Propagators and spectra of surface polaritons in metallic slabs: Effects of quantum-mechanical nonlocality

V. Despoja* and M. Šunjić†
Department of Physics, University of Zagreb, Bijenička 32, HR-10000 Zagreb, Croatia

L. Marušić‡
Department of Transport and Maritime Studies, University of Zadar, M. Pavlinovića b.b., HR-23000 Zadar, Croatia

(Received 26 March 2009; revised manuscript received 30 May 2009; published 7 August 2009)

A transparent and compact method for the calculation of the electromagnetic-field propagator in presence of a thin metallic slab is developed. Electron wave functions for the slab are obtained numerically by using density-functional theory within the local density approximation, and used to construct the slab conductivity tensor. Expressions for the free-photon Green's function and photon self-energy (i.e., slab conductivity tensor) in terms of electronic wave functions are derived analytically, taking advantage of the symmetry of the problem and separating it in *s* and *p* polarizations. Dyson equation for the polariton propagator is analytically prepared to be solved in two steps: first, solving the Dyson equation with only paramagnetic (nonlocal) part of photon self-energy included, and second, renormalizing such propagator because of its interaction with diamagnetic (local) polarizations. Such approach allows us to take both polarization mechanisms into account as well as their mutual influence. Long-wavelength and quasistatic limits of our results are derived and compared with previous results. Finally, the method is used to calculate spectra of polaritons, i.e., electromagnetic excitations produced by an oscillating dipole placed in the vicinity or inside a metallic slab.

DOI: 10.1103/PhysRevB.80.075410 PACS number(s): 73.20.Mf, 71.36.+c

I. INTRODUCTION

Theoretical description of optical properties of metallic surfaces made significant progress in the late fifties when, e.g., surface plasmon oscillations in metallic films were discovered[1,2] and explained using a simple electrostatic theory. In late sixties Economou[3] calculated dispersion relations of surface plasmon polaritons in metallic slabs by solving the complete set of Maxwell equations, but using a local dielectric function $\epsilon(\omega)$. First calculations which include microscopic structure in a semi-infinite metal, i.e., solutions of the microscopic Maxwell equations with nonlocal conductivity tensor $\sigma_{\mu\nu}(Q,\omega,z,z')$ were performed in the seventies by Feibelman[4] who used *jellium* model and surface barrier potential of Lang and Kohn.[5] Nevertheless, he used a semilocal approximation with nonlocal tensor $\sigma_{\mu\nu}$ and the bulk dielectric function $\epsilon(\mathbf{k},\omega)$. He used a similar formulation to demonstrate that the electric field of the *p*-polarized incident electromagnetic wave is enhanced in the surface region, and that the enhancement strongly depends on the shape of the surface barrier potential.[6] This result is very useful even today for the description of many physical problems such as photoemission from metallic surfaces, surface enhanced absorption/emission in molecules, Raman scattering, etc. In Sec. V we confirm his results by a much more elaborate calculation.

More recently, plasmon pole and semilocal approximations were used to calculate the propagator of electromagnetic field in infinite and semi-infinite metals.[7] Keller and Liu[8] also calculated reflection coefficients for *s*- and *p*-polarized electromagnetic fields for ultrathin metallic films when only diamagnetic part of the conductivity tensor $\sigma_{\mu\nu}$ is included. Same authors calculated paramagnetic response of ultrathin semiconductor quantum well (QW) with only two levels related to the motion perpendicular to the surfaces (one occupied and one unoccupied).[9] In this paper we use their formal expression for the nonlocal conductivity tensor in QW to derive analytical expression for the conductivity tensor and compare it with their results in the long-wavelength limit $\sigma_{\mu\nu}(Q\rightarrow 0,\omega,z,z')$.

Excitation spectra calculated in Ref. 9 have a sharp peak corresponding to the blueshifted interband transition. The same blueshift is registered in our calculations and presented in Sec. V. Thickness-dependent oscillations in reflectivity coefficient measured for Al i Cu films[10] are probably caused by the same interband transitions. At the same time, an advanced theory has been developed to include nonlinear optical response, e.g., second-order response phenomenon such as photon drag current,[11] Raman scattering[12] or two photon photoemission[13] and third-order response phenomenon as optical phase conjugated field.[14]

In the last decade, most effort has been dedicated to experimental investigations of the interplay between enhanced emission and nonradiative resonant energy transfer to surface polaritons (quenching of emission) in a system consisting of an excited molecule or excitons in a semiconductor and a metallic surface. Examples of such systems are: enhanced decay of excitons in a semiconductor QW into surface polaritons in thin metallic films,[15–17] decay of excited organic molecule near thin noble metal films,[18,19] and thickness-dependent transition from enhancement to quenching of emission of a quantum dot on a gold film.[20]

There have been comprehensive experimental measurements of enhanced luminescence of single organic molecule in the vicinity of gold/silver nanoparticles. Such nanoparticles amplify the efficiency of energy transfer from an excited molecule into radiation, i.e., act as some kind of nanoantenna.[21–23] At smaller distances between a molecule and a metal nanoparticle, resonant energy transfer into surface plasmon in a metal occurs, but without emission (fluo-

rescence quenching). Experimental evidence of emission quenching has been detected for an excited molecule near a spherical gold nanoparticle[24] and for a quantum dot near a spherical gold nanoparticle.[25] Finally, transition from enhancement into quenching as a function of single-molecule gold-nanoparticle separation has been measured.[26]

Theoretical descriptions of such phenomena are scarce. Existing theories mostly do not include the retardation effect which makes it impossible to analyze the radiative decay channel. Moreover, microscopic electronic excitation in metallic nanostructures are treated in a local[27,28] or a semilocal[29] approximation which does not enable correct description of nonradiative decay channel at short distances (e.g., local theory is not sufficient to describe fluorescence quenching at short distances[26]). Retardation effects were included, e.g., in the calculation of decay of excited molecule interacting with metallic surface excitations[30,31] but metal was still treated as a dielectric medium described with a local dielectric function $\epsilon(\omega)$.

Furthermore, some previous *ab initio* calculations suggest that realistic band structure could be very important in the description of optical phenomena near metallic surfaces. For example, inclusion of the real band structure even for simple metallic surfaces such as Mg(0001)[32] or Be(0001)[33] strongly modifies energy and width of surface plasmons in the long-wavelength limit, which can cause significant modification of coupling of the surface plasmons to the external radiation. Inclusion of band structure also leads to the appearance of new collective modes—acoustic plasmons[34,35] with linear ($\omega \sim Q$) instead of usual square root ($\omega \sim \sqrt{Q}$) surface plasmon dispersion. Acoustic plasmon even lower below the light line (Qc) opens a new coupling channel of radiation to surfaces. *Ab initio* calculations for simple metal monolayers (for example, beryllium monolayer[36] which corresponds to ultrathin metallic slab used as a model here) show that there are four instead of two surface plasmons. Also, because of, continuum interband electron-hole transitions intraband plasmon is damped much before entering into intraband electron-hole continuum. All this suggest that in addition to retardation effects, band-structure effects are also important.

Hence, for the proper description of enhanced radiative/nonradiative decay mechanisms of an excited molecule or excitons near a metallic surface and similar processes we need a theory which includes both, correct description of retarded electromagnetic field and a quantum-mechanical nonlocality. This is the main motivation to extend our previous theoretical formalism based on the propagator of screened dynamical Coulomb (nonretarded) interaction $W(Q,\omega,z,z')$ [solution of a microscopic Poisson equation which includes nonlocal density response function $R(Q,\omega,z,z')$ (Refs. 37 and 38)] to the propagator of the electromagnetic field $D_{\mu\nu}(Q,\omega,z,z')$ [solution of complete set of microscopic Maxwell equations which include nonlocal conductivity tensor $\sigma_{\mu\nu}(Q,\omega,z,z')$].

In Sec. II we present the construction of the photon propagator $D_{\mu\nu}(Q,\omega,z,z')$ in terms of Dyson equation, using Feynman perturbation expansion. We expand $D_{\mu\nu}$ in terms of free-photon propagator $D^0_{\mu\nu}$ and photon self-energy $\Pi_{\mu\nu}(Q,\omega,z,z')$, which is proportional to the conductivity tensor $\sigma_{\mu\nu}(Q,\omega,z,z')$.

In Sec. III we examine the validity of our results by exploring their limits. We compare the quasistatic limit for $D^0_{\mu\nu}$ and the long-wavelength limit for $\Pi_{\mu\nu}$ with well-known expressions in Refs. 9 and 39, respectively.

In Sec. IV we present the calculation of the electromagnetic propagator $D_{\mu\nu}$ from the expressions derived in Sec. II. In order to make the calculation numerically efficient we take into account that the self-energy term $\Pi_{\mu\nu}$ consists of a local (diamagnetic) and a nonlocal (paramagnetic) part, and solve the Dyson equation in two steps. The first step, described in Sec. IV A, is to solve the equation including only paramagnetic polarizability while the diamagnetic polarizability is neglected and obtain the propagator $D^{para}_{\mu\nu}$. The second step, described in Sec. IV B is to renormalize this propagator because of the interaction with diamagnetic excitations. This method of solution is also useful from the physical point of view because it allows us the detailed investigation of each polarization mechanism separately, as well as their mutual influence. Finally, formal extension towards inclusion of band-structure effects in our formulation is briefly presented in Sec. IV C.

In Sec. V we apply the developed formalism to a few standard situations. We first use the propagator $D_{\mu\nu}$ to calculate the spectra of electromagnetic excitations, i.e., radiative and nonradiative polaritons, by coupling them to an oscillating dipole placed inside or outside of a metallic slab. We analyze the spectra to determine the paramagnetic and diamagnetic contributions as well as the importance of their mutual influence. We also compare our results with the classical ones by replacing our quantum-mechanical description based on the local dielectric function $\epsilon(\omega,z)$ with the classical description where the dielectric function is $\epsilon(\omega)$ inside the slab and equal to one outside. It is interesting that even in the long-wavelength limit quantum-mechanical effects modify the classical description and electron interband transitions appear in the polariton spectra. Finally, we study the shape of the electric field produced by a dipolar probe placed, e.g., inside the slab, and find the expected strong enhancement in the radiative region.

II. FORMULATION OF THE PROBLEM

A. Description of the system

Our system consists of electrons in a thin metallic slab coupled to electromagnetic fields. The slab is described as jellium of thickness d, and the coordinate system is chosen so that the slab is infinite in $\rho=(x,y)$ direction while in z direction it is positioned between $-L$ and 0, where $L=d+2\Delta$ and Δ is chosen so that electron density at such distance from the jellium is negligible compared to its maximum value. This means that electron density practically vanishes in $-L$ and 0, while the jellium is positioned between $-L+\Delta$ and $-\Delta$ (Fig. 1). The electromagnetic fields can be produced by sources located inside or outside the slab. The Hamiltonian of the system can be written as

$$H = H_0 + V \tag{1}$$

Unperturbed Hamiltonian H_0 consist of two parts

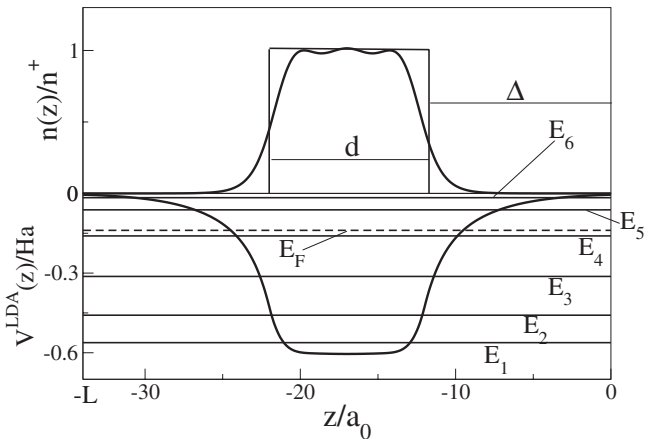

FIG. 1. Electronic density, energy levels, and self-consistent LDA potential for our model system. Positive background thickness is $10a_0$ and $r_s=2$. Electronic density is nonzero in the interval $-L<z<0$, where $L=34a_0$.

$$H_0 = H_0^e + H_0^{EM}$$

H_0^e describes electrons in the self-consistent Kohn-Sham local density approximation (KS-LDA) potential[40] (illustrated in Fig. 1) and H_0^{EM} describes the electromagnetic field in vacuum. V is the interaction between the KS-LDA electrons in a metallic slab and the electromagnetic field, which by using $\Phi=0$ gauge can be written as

$$V = -\frac{1}{c}\int d\mathbf{r}\mathbf{J}(\mathbf{r})\mathbf{A}(\mathbf{r}), \tag{2}$$

where

$$\mathbf{J}(\mathbf{r}) = \frac{e\hbar}{2im}\left\{\psi^+(\mathbf{r})\nabla\psi(\mathbf{r}) - [\nabla\psi^+(\mathbf{r})]\psi(\mathbf{r}) - \frac{ie}{\hbar c}\mathbf{A}(\mathbf{r})\psi^+(\mathbf{r})\psi(\mathbf{r})\right\}. \tag{3}$$

Now V can be divided into two terms[41]

$$V = V^{dia} + V^{para},$$

where

$$V^{dia} = \frac{e^2}{2mc^2}\int d\mathbf{r}\rho(\mathbf{r})\mathbf{A}^2(\mathbf{r}) \tag{4}$$

is the diamagnetic interaction of the electromagnetic field $\mathbf{A}$ with the density fluctuations in the slab, and

$$V^{para} = -\frac{1}{c}\int d\mathbf{r}\mathbf{j}(\mathbf{r})\mathbf{A}(\mathbf{r}) \tag{5}$$

is the paramagnetic interaction of the electromagnetic field with the current fluctuations $\mathbf{j}(\mathbf{r})$ in the slab. Electron density and current operators in Eqs. (4) and (5) are now defined as

$$\rho(\mathbf{r}) = \psi^+(\mathbf{r})\psi(\mathbf{r})$$

$$\mathbf{j}(\mathbf{r}) = \frac{e\hbar}{2im}\{\psi^+(\mathbf{r})\nabla\psi(\mathbf{r}) - [\nabla\psi^+(\mathbf{r})]\psi(\mathbf{r})\},$$

where the field operators are

$$\psi^+(\mathbf{r}) = \frac{1}{\sqrt{S}}\sum_{n,\mathbf{K}}\phi_n(z)e^{i\mathbf{K}\boldsymbol{\rho}}c^+_{n\mathbf{K}}. \tag{6}$$

Here $c^+_{n\mathbf{K}}$ is the creation operator of an electron in the KS-LDA state $\{n,\mathbf{K}\}$, with the (real) wave function in z direction $\phi_n(z)$ and energy E_n, while $\mathbf{K}$ is the electron wave vector component parallel to the surface. It is important to mention that the longitudinal part of the vector potential $\mathbf{A}$ equal to zero in the Coulomb gauge now plays a role identical to the scalar potential in the Coulomb gauge, i.e., it replaces the instantaneous (Coulomb) interaction between charges. Therefore, vector potential $\mathbf{A}$, related to the electric field as

$$\mathbf{E}(\mathbf{r},t) = -\frac{1}{c}\frac{\partial\mathbf{A}(\mathbf{r})}{\partial t}, \tag{7}$$

can be used to fully describe all electromagnetic phenomena.

B. Definition of the propagator

Free-photon Green's function or propagator can be defined as[42]

$$D^0_{\mu\nu}(\mathbf{r},\mathbf{r}',t,t') = \frac{i}{\hbar c}\theta(t-t')\langle\Psi^0_{EM}|[A^0_\mu(\mathbf{r},t),A^0_\nu(\mathbf{r}',t')]_-|\Psi^0_{EM}\rangle, \tag{8}$$

where $\mu,\nu=x,y,z$, the state Ψ^0_{EM} is the photon vacuum (ground state of H_0^{EM}), and the operator A^0 is defined as

$$A^0_\mu(\mathbf{r},t) = e^{iH_0t}A_\mu(\mathbf{r})e^{-iH_0t}.$$

To take the interaction with electronic excitations into account, we need to calculate the retarded photon Green's function defined as

$$D_{\mu\nu}(\mathbf{r},\mathbf{r}',t,t') = \frac{i}{\hbar c}\theta(t-t')\langle\Psi|[A_\mu(\mathbf{r},t),A_\nu(\mathbf{r}',t')]_-|\Psi\rangle, \tag{9}$$

where

$$|\Psi\rangle = |\Psi_e;\Psi_{EM}\rangle$$

represents the ground state of interacting electron and photon systems, i.e., the ground state of the full Hamiltonian (1), and the operator A is defined as

$$A_\mu(\mathbf{r},t) = e^{iHt}A_\mu(\mathbf{r})e^{-iHt}.$$

If we restrict ourselves to the RPA-type diagrams, the propagator $D_{\mu\nu}$ in Eq. (9) can be obtained from the perturbation expansion shown in Fig. 2, leading to the Dyson equation shown in Fig. 3.

The second term [Fig. 2(b)] is first order in perturbation V^{dia} and contains the self-energy term

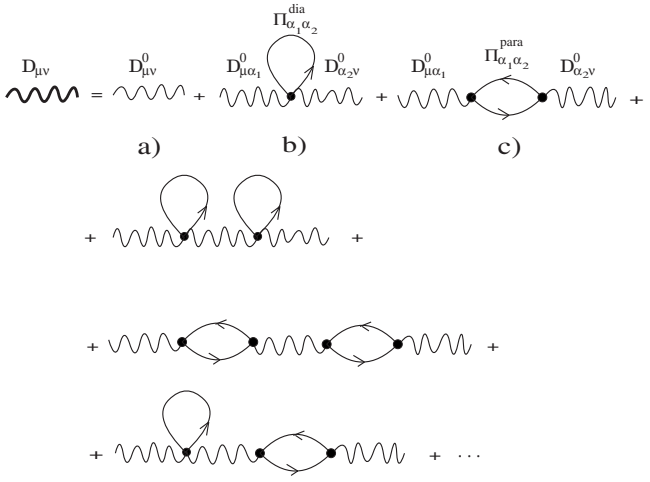

FIG. 2. Perturbation expansion for the photon propagator $D_{\mu\nu}$.

$$\Pi^{dia}_{\mu\nu}(\mathbf{r},\mathbf{r}',t,t') = -\frac{e^2}{mc}\langle\rho(\mathbf{r})\rangle\delta(t-t')\delta(\mathbf{r}-\mathbf{r}')\delta_{\mu\nu}, \quad (10)$$

where $\langle\rho(\mathbf{r})\rangle = \langle\Psi^0_e|\rho(\mathbf{r})|\Psi^0_e\rangle$ is the ground-state electron density. $|\Psi^0_e\rangle$ is the LDA ground state, i.e., ground state of the Hamiltonian H^e_0. Self-energy term (10) represents the diamagnetic response of the metallic slab to the external field.

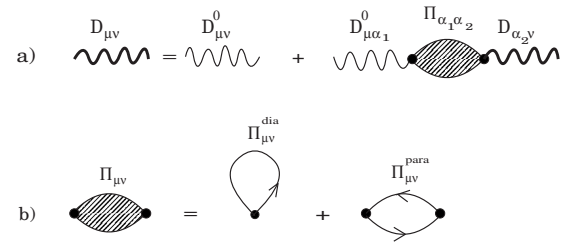

FIG. 3. (a) Dyson equation for the photon propagator; (b) RPA photon self-energy diagrams.

This response is local, isotropic and depends only on the local electron density.

The third term [Fig. 2(c)] is second order in the perturbation V^{para} and contains the self-energy term

$$\Pi^{para}_{\mu\nu}(\mathbf{r},\mathbf{r}',t,t') = \frac{i}{\hbar c}\theta(t-t')\langle\Psi^0_e|[j_\mu(\mathbf{r},t),j_\nu(\mathbf{r}',t')]_-|\Psi^0_e\rangle \quad (11)$$

which is the current-current response function and represents the paramagnetic response of a slab to the external electromagnetic field.

Figure 3(a) represents the Dyson equation for the photon propagator $D_{\mu\nu}$ which, after Fourier transformation with respect to time and direction parallel to the surface, becomes

$$D_{\mu\nu}(\mathbf{Q},\omega,z,z') = D^0_{\mu\nu}(\mathbf{Q},\omega,z,z') + \sum_{\alpha_1}\sum_{\alpha_2}\int_{-L}^{0} dz_1 \int_{-L}^{0} dz_2 D^0_{\mu\alpha_1}(\mathbf{Q},\omega,z,z_1)\Pi_{\alpha_1\alpha_2}(\mathbf{Q},\omega,z_1,z_2)D_{\alpha_2\nu}(\mathbf{Q},\omega,z_2,z'), \quad (12)$$

where $\mathbf{Q}$ is the wave vector parallel to the surface. Introducing two-dimensional matrices $M_{\mu\nu}$ of the form

$$\hat{\mathbf{M}} = \begin{bmatrix} M_{xx} & M_{xy} & M_{xz} \\ M_{yx} & M_{yy} & M_{yz} \\ M_{zx} & M_{zy} & M_{zz} \end{bmatrix}.$$

Equation (12) can be written in the matrix form

$$\hat{\mathbf{D}} = \hat{\mathbf{D}}^0 + \hat{\mathbf{D}}^0 \otimes \hat{\mathbf{\Pi}} \otimes \hat{\mathbf{D}}, \quad (13)$$

where the symbol $\otimes$ denotes the convolution with respect to the variable of integration (z_1 or z_2) in addition to the matrix multiplication.

C. Calculation of the self-energy diagrams

Photon self-energy matrix $\mathbf{\Pi}$, illustrated in Fig. 3(b), has the form

$$\hat{\mathbf{\Pi}} = \hat{\mathbf{\Pi}}^{dia} + \hat{\mathbf{\Pi}}^{para}, \quad (14)$$

where the diamagnetic term is a function of the LDA density profile $n(z)$ shown in Fig. 1

$$\hat{\mathbf{\Pi}}^{dia}(Q,\omega,z,z') = -\frac{e^2}{mc}n(z)\delta(z-z')\hat{\mathbf{I}} \quad (15)$$

and $\hat{\mathbf{I}}$ is the unit matrix.

To calculate the matrix elements of $\hat{\mathbf{\Pi}}^{para}$ we start from Eq. (11). Using the definitions Eqs. (5) and (6), and Fourier transforming, current-current response function for the metallic slab becomes

$$\Pi^{para}_{\mu\nu}(\mathbf{Q},\omega,z,z') = -\frac{2}{c}\sum_{\mathbf{K}nm}\frac{f_n(\mathbf{K}) - f_m(\mathbf{K}+\mathbf{Q})}{\hbar(\omega+i\eta) + E_n(\mathbf{K}) - E_m(\mathbf{K}+\mathbf{Q})} \times j^\mu_{nm}(2\mathbf{K}+\mathbf{Q},z)j^\nu_{mn}(2\mathbf{K}+\mathbf{Q},z'), \quad (16)$$

where $E_n(\mathbf{K}) = E_n + \frac{\hbar^2K^2}{2m}$, and the Fourier transform of the current density producing the transition from state $\{n,\mathbf{K}\}$ to $\{m,\mathbf{K}+\mathbf{Q}\}$ is[14]

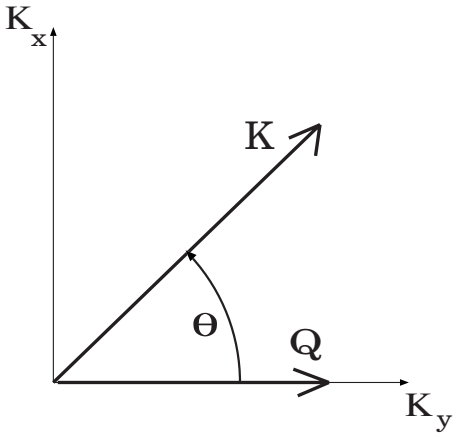

FIG. 4. Choice of **K** and **Q** wave vectors.

$$\mathbf{j}_{nm}(2\mathbf{K}+\mathbf{Q},z)=\frac{e\hbar}{2im}\{i\phi_n(z)\phi_m(z)(2\mathbf{K}+\mathbf{Q}) + [\phi_n(z)\partial_z\phi_m(z)-\phi_m(z)\partial_z\phi_n(z)]\hat{\mathbf{z}}\}. \tag{17}$$

The first and second terms in Eq. (17) represent the currents parallel and perpendicular to the surface, respectively.

Because of the isotropy of our system in the plane parallel to the surface the directions of x and y axes are arbitrary, enabling us to choose the vector **Q** to be parallel to K_y, as shown in Fig. 4. In that case $\hat{\mathbf{\Pi}}^{para}$ can be written as

$$\hat{\mathbf{\Pi}}^{para}(z,z')=\sum_{nm}\hat{\boldsymbol{\rho}}_{nm}(z)\hat{\mathbf{F}}_{nm}\hat{\boldsymbol{\rho}}_{nm}(z'), \tag{18}$$

where

$$\hat{\boldsymbol{\rho}}_{nm}(z)=\begin{bmatrix}\rho_{nm}(z) & 0 & 0\\ 0 & \rho_{nm}(z) & 0\\ 0 & 0 & j_{nm}(z)\end{bmatrix}, \tag{19}$$

with the notation

$$\rho_{nm}(z)=\phi_n(z)\phi_m(z)$$

and

$$j_{nm}(z)=\phi_n(z)\partial_z\phi_m(z)-\phi_m(z)\partial_z\phi_n(z),$$

while the matrix $\hat{\mathbf{F}}$ has the following form:

$$\hat{\mathbf{F}}_{nm}=\begin{bmatrix}F_{nm}^{xx} & 0 & 0\\ 0 & F_{nm}^{yy} & F_{nm}^{yz}\\ 0 & F_{nm}^{zy} & F_{nm}^{zz}\end{bmatrix}. \tag{20}$$

Functions $F_{nm}^{\mu\nu}$ can be obtained analytically, and the explicit expressions together with the detailed calculations are presented in Appendix A.

With the same choice of the vector **Q**, free-photon propagator $D_{\mu\nu}^0$ can be written in the form

$$\hat{\mathbf{D}}^0=\begin{bmatrix}D_{xx}^0 & 0 & 0\\ 0 & D_{yy}^0 & D_{yz}^0\\ 0 & D_{zy}^0 & D_{zz}^0\end{bmatrix}, \tag{21}$$

where

$$D_{xx}^0(Q,\omega,z,z')=\frac{2\pi i}{ck_\perp}e^{ik_\perp|z-z'|}, \tag{22}$$

$$D_{yy}^0(Q,\omega,z,z')=\frac{2\pi ick_\perp}{\omega^2}e^{ik_\perp|z-z'|}, \tag{23}$$

$$D_{zz}^0(Q,\omega,z,z')=-\frac{4\pi c}{\omega^2}\delta(z-z')+\frac{2\pi icQ^2}{k_\perp\omega^2}e^{ik_\perp|z-z'|}, \tag{24}$$

and

$$D_{yz}^0(Q,\omega,z,z')=D_{zy}^0(Q,\omega,z,z') =-\frac{2\pi icQ}{\omega^2}sgn(z-z')e^{ik_\perp|z-z'|}. \tag{25}$$

Here $k_\perp=\sqrt{K_0^2-Q^2}$ is the perpendicular wave vector. Detailed calculations are presented in Appendix B.

Assuming that we have the s-polarized test field (oriented in x direction) then the induced electromagnetic field is, in vacuum, propagated by D_{xx}^0. Similarly, if the test field is p polarized (in the y-z plane) the produced electromagnetic field is propagated in vacuum by D_{yy}^0, D_{zz}^0, D_{yz}^0, and D_{zy}^0 (as will be demonstrated in the following section). However, since the tensors $\mathbf{\Pi}$ and $\mathbf{D}^0$ have the same structure, it is obvious that the s-polarized external field will induce only s-polarized density/current fluctuations in the slab while the p-polarized external field will induce only p-polarized density/current fluctuations. In other words, s- and p-polarized electromagnetic modes never mix, so that the matrices $\mathbf{D}^0$ and $\mathbf{\Pi}$ can be rearranged in s and p blocks

$$\hat{\mathbf{D}}^0=\begin{bmatrix}D_s^0 & 0\\ 0 & \hat{\mathbf{D}}_p^0\end{bmatrix},\quad \hat{\mathbf{\Pi}}=\begin{bmatrix}\Pi_s & 0\\ 0 & \hat{\mathbf{\Pi}}_p\end{bmatrix},$$

where

$$D_s^0=D_{xx}^0,\quad \hat{\mathbf{D}}_p^0=\begin{bmatrix}D_{yy}^0 & D_{yz}^0\\ D_{zy}^0 & D_{zz}^0\end{bmatrix},$$

and

$$\Pi_s=\Pi_{xx},\quad \hat{\mathbf{\Pi}}_p=\begin{bmatrix}\Pi_{yy} & \Pi_{yz}\\ \Pi_{zy} & \Pi_{zz}\end{bmatrix}.$$

This enables us to separate the Dyson Eq. (12) into two independent equations for s- and p-polarized fields.

Before proceeding with the solution of the Dyson equation, let us examine the long-wavelength ($Q\to 0$) limit of the self-energy $\hat{\mathbf{\Pi}}$ and the quasistatic limit of the propagator $\hat{\mathbf{D}}^0$, and compare them with the standard results.

III. LIMITS

We want to compare our results with the previously obtained ones, checking the long-wavelength (classical) and nonretarded limits. Specifically, we show that the result for the self-energy $\hat{\mathbf{\Pi}}$ in the long-wavelength limit ($Q\to 0$) reduces to the previous results,[4–9] and that the free-photon propagator $\hat{\mathbf{D}}^0$ in the quasistatic ($c\to\infty$) limit leads to the correct electric field.[39]

A. Long-wavelength limit of the self-energy $\hat{\Pi}$

Induced current produced by the external vector potential is defined as

$$j_\mu^{ind}(Q,\omega,z) = \int dz_1 \Pi_{\mu\nu}(Q,\omega,z,z_1) A_\nu^{ext}(Q,\omega,z_1).$$

Using the Fourier transform of Eq. (7)

$$A_\nu^{ext}(Q,\omega,z_1) = -\frac{ic}{\omega} E_\nu^{ext}(Q,\omega,z_1)$$

induced current can be related to the external electric field as

$$j_\mu^{ind}(Q,\omega,z) = -i\frac{c}{\omega}\int dz_1 \Pi_{\mu\nu}(Q,\omega,z,z_1) E_\nu^{ext}(Q,\omega,z_1)$$

and the electric conductivity tensor is therefore

$$\sigma_{\mu\nu}(Q,\omega,z,z') = -i\frac{c}{\omega}\Pi_{\mu\nu}(Q,\omega,z,z').$$

Knowing the expected properties of $\sigma_{\mu\nu}$ in our system we can verify the correct behavior of $\Pi_{\mu\nu}$ in the long-wavelength limit.

If we apply a uniform (i.e., $Q\to 0$) electric field in x direction it will induce the current only in x direction. Due to isotropy in (x,y) plane, if we apply the same electric field in y direction it will induce exactly the same current in y direction. However, if that same electric field is in z direction it will induce the current in the z direction but with different magnitude. This leads to the conclusion that for $Q\to 0$ we should obtain

$$\Pi_{xx}(Q\to 0,\omega,z,z') = \Pi_{yy}(Q\to 0,\omega,z,z') \neq \Pi_{zz}(Q\to 0,\omega,z,z')$$

and

$$\Pi_{xz}(Q\to 0,\omega,z,z') = \Pi_{zx}(Q\to 0,\omega,z,z') = 0.$$

Indeed, our results for the diagonal elements of $\hat{\mathbf{\Pi}}$ (derived in Appendix A) in the long-wavelength limit become

$$\Pi_{xx}(Q\to 0,\omega,z,z') = \Pi_{yy}(Q\to 0,\omega,z,z') = -\frac{\omega_p^2}{4\pi c}\frac{n(z)}{n^+}\delta(z-z') - \frac{\hbar^2 e^2}{8\pi m^2 c}\sum_{n=1}^{N_{occ}}[K_F^n]^4 \times \sum_{m=1}^{\infty}\left\{\frac{1}{\hbar(\omega+i\eta)+E_n-E_m} - \frac{1}{\hbar(\omega+i\eta)+E_m-E_n}\right\}\rho_{nm}(z)\rho_{nm}(z')$$

and

$$\Pi_{zz}(Q\to 0,\omega,z,z') = -\frac{\omega_p^2}{4\pi c}\frac{n(z)}{n^+}\delta(z-z') - \frac{\hbar^2 e^2}{8\pi m^2 c}\sum_{n=1}^{N_{occ}}[K_F^n]^2\sum_{m=1}^{\infty}\left\{\frac{1}{\hbar(\omega+i\eta)+E_n-E_m} - \frac{1}{\hbar(\omega+i\eta)+E_m-E_n}\right\}j_{nm}(z)j_{nm}(z')$$

Also, the components Π_{yz} and Π_{zy} in $Q\to 0$ limit disappear linearly with Q. This long-wavelength limit of the electric conductivity tensor $\sigma_{\mu\nu}(Q\to 0,\omega,z,z') = -i\frac{c}{\omega}\Pi_{\mu\nu}(Q\to 0,\omega,z,z')$ is in accordance with previous calculations.[9]

B. Quasistatic limit of the propagator $\hat{\mathbf{D}}^0$

For an external current distribution oriented in the y direction $j_y^{ext}(\mathbf{Q},\omega,z_1)$ the produced electric field can be written using Eqs. (21) and (B1) as

$$\mathbf{E}(Q,\omega,z) = i\frac{\omega}{c}\int dz_1 [D_{yy}^0(Q,\omega,z,z_1)\mathbf{y} + D_{zy}^0(Q,\omega,z,z_1)\mathbf{z}] j_y^{ext}(\mathbf{Q},\omega,z_1). \quad (26)$$

After inserting Eqs. (22) and (25) we get

$$\mathbf{E}(Q,\omega,z) = -\frac{2\pi}{\omega}\int dz_1 [k_\perp \mathbf{y} - Q\, sgn(z-z_1)\mathbf{z}] e^{ik_\perp|z-z_1|} j_y^{ext}(\mathbf{Q},\omega,z_1). \quad (27)$$

In the quasistatic limit $c\to\infty$ and $k_\perp \to iQ$ and expression (27) becomes

$$\mathbf{E}(Q,\omega,z) = -\left[iQ\mathbf{y} + \frac{\partial}{\partial z}\mathbf{z}\right]\frac{2\pi}{\omega}\int dz_1 e^{-Q|z-z_1|} j_y^{ext}(\mathbf{Q},\omega,z_1). \quad (28)$$

Moreover, if we use the continuity Eq. (B5) we get

$$j_y^{ext}(\mathbf{Q},\omega,z_1) = \frac{\omega}{Q}\rho^{ext}(\mathbf{Q},\omega,z_1).$$

Finally, after using this expression in Eq. (28) we get the well-known result for the electric field in the electrostatic limit[39]

$$\mathbf{E}(Q,\omega,z) = -\left[iQ\mathbf{y} + \frac{\partial}{\partial z}\mathbf{z}\right]\int dz_1 \frac{2\pi}{Q} e^{-Q|z-z_1|}\rho^{ext}(\mathbf{Q},\omega,z_1) \quad (29)$$

i.e., $\mathbf{E}=-\nabla\Phi^{ext}$, which proves that $\hat{\mathbf{D}}^0$ behaves correctly in the quasistatic limit.

IV. SOLUTION OF THE DYSON EQUATION

In Sec. II we obtained the self-energy $\hat{\mathbf{\Pi}}$ and the free-photon propagator $\hat{\mathbf{D}}^0$ and we can use them to solve the

Dyson Eq. (12) and (13). Since $\hat{\mathbf{\Pi}}^{dia}$ contribution to self-energy is local while $\hat{\mathbf{\Pi}}^{para}$ contribution is nonlocal, they should be treated differently from the numerical point of view. We shall perform the numerical solution of the Dyson equation in two steps. First, we shall solve the Dyson equation with only the paramagnetic contribution included (i.e., $\hat{\mathbf{\Pi}}=\hat{\mathbf{\Pi}}^{para}$), and then use this solution as a starting point to solve the complete Dyson equation by treating the diamagnetic term as a perturbation. This procedure is very useful, not only because of its numerical efficiency but also because it enables us to investigate the behavior of each of the polarization mechanisms (current fluctuations caused by electron-hole excitations and density fluctuations) separately, as well as their influence on each other, as presented in Sec. V.

Since the photon self-energy consists of diamagnetic and paramagnetic contributions, the equation can be symbolically written as

$$\hat{\mathbf{D}} = \hat{\mathbf{D}}^0 + \hat{\mathbf{D}}^0 \otimes \hat{\mathbf{\Pi}}^{dia} \otimes \hat{\mathbf{D}} + \hat{\mathbf{D}}^0 \otimes \hat{\mathbf{\Pi}}^{para} \otimes \hat{\mathbf{D}}$$

which can be rearranged as

$$(\hat{\mathbf{I}} - \hat{\mathbf{D}}^0 \otimes \hat{\mathbf{\Pi}}^{para}) \otimes \hat{\mathbf{D}} = \hat{\mathbf{D}}^0 + \hat{\mathbf{D}}^0 \otimes \hat{\mathbf{\Pi}}^{dia} \otimes \hat{\mathbf{D}}.$$

After multiplying from the left with inverse matrix $(\hat{\mathbf{I}}-\hat{\mathbf{D}}^0 \otimes \hat{\mathbf{\Pi}}^{para})^{-1}$ we get

$$\hat{\mathbf{D}} = (\hat{\mathbf{I}} - \hat{\mathbf{D}}^0 \otimes \hat{\mathbf{\Pi}}^{para})^{-1} \otimes \hat{\mathbf{D}}^0 + (\hat{\mathbf{I}} - \hat{\mathbf{D}}^0 \otimes \hat{\mathbf{\Pi}}^{para})^{-1} \otimes \hat{\mathbf{D}}^0 \otimes \hat{\mathbf{\Pi}}^{dia} \otimes \hat{\mathbf{D}}.$$

By introducing notation

$$\hat{\mathbf{D}}^{para} = (\hat{\mathbf{I}} - \hat{\mathbf{D}}^0 \otimes \hat{\mathbf{\Pi}}^{para})^{-1} \otimes \hat{\mathbf{D}}^0 \tag{30}$$

we finally get

$$\hat{\mathbf{D}} = \hat{\mathbf{D}}^{para} + \hat{\mathbf{D}}^{para} \otimes \hat{\mathbf{\Pi}}^{dia} \otimes \hat{\mathbf{D}}. \tag{31}$$

It is obvious from Eq. (30) that $\hat{\mathbf{D}}^{para}$ is the solution of equation

$$\hat{\mathbf{D}}^{para} = \hat{\mathbf{D}}^0 + \hat{\mathbf{D}}^0 \otimes \hat{\mathbf{\Pi}}^{para} \otimes \hat{\mathbf{D}}^{para}. \tag{32}$$

This is the photon propagator for photons interacting only with the paramagnetic polarization. The full propagator can be obtained by solving the Eq. (31).

Similar treatment of the Dyson equation has already been used to calculate the propagator of screened Coulomb interaction in a polarizable system described by irreducible polarizability P^2 placed in the vicinity of another polarizable system described by irreducible polarizability P^1.[43]

A. Paramagnetic contribution

With the help of Eq. (18), Eq. (32) becomes

$$\hat{\mathbf{D}}^{para} = \hat{\mathbf{D}}^0 + \sum_{nm} \hat{\mathbf{D}}^0 \otimes \hat{\boldsymbol{\rho}}_{nm} \hat{\mathbf{F}}_{nm} \hat{\boldsymbol{\rho}}_{nm} \otimes \hat{\mathbf{D}}^{para}. \tag{33}$$

This set of integral equations can be transformed into matrix equations by acting from the left with $\hat{\boldsymbol{\rho}}_{nm}\otimes$ and rearranging to get the equation for $\hat{\boldsymbol{\rho}}_{nm}\otimes\hat{\mathbf{D}}^{para}$

$$\hat{\boldsymbol{\rho}}_{nm} \otimes \hat{\mathbf{D}}^{para} = \hat{\boldsymbol{\rho}}_{nm} \otimes \hat{\mathbf{D}}^0 + \sum_{n'm'} [\hat{\boldsymbol{\rho}}_{nm} \otimes \hat{\mathbf{D}}^0 \otimes \hat{\boldsymbol{\rho}}_{n'm'} \hat{\mathbf{F}}_{n'm'}] \hat{\boldsymbol{\rho}}_{n'm'} \otimes \hat{\mathbf{D}}^{para}. \tag{34}$$

This is now a set of five matrix equations for $[\hat{\boldsymbol{\rho}}_{nm} \otimes \hat{\mathbf{D}}^{para}]_{\mu\nu}$ with solutions for the **s** polarization

$$\boldsymbol{\rho}^{xx}_{nm} \otimes D^{para}_{xx} = \sum_{n'm'} [S^{-1}]_{nm,n'm'} \boldsymbol{\rho}^{xx}_{n'm'} \otimes D^0_{xx} \tag{35}$$

and for the **p** polarization

$$[\hat{\boldsymbol{\rho}}_{nm} \otimes \hat{\mathbf{D}}^{para}]_{\mu\nu} = \sum_{n'm',\alpha} [\hat{\mathbf{P}}^{-1}]^{\mu\alpha}_{nm,n'm'} [\hat{\boldsymbol{\rho}}_{n'm'} \otimes \hat{\mathbf{D}}^0]_{\alpha\nu}; \quad \mu,\nu = y,z, \tag{36}$$

where we introduce matrices $S=T^{xx}$ and

$$\hat{\mathbf{P}} = \begin{bmatrix} T^{yy} & T^{yz} \\ T^{zy} & T^{zz} \end{bmatrix}.$$

and where the matrix elements of the $T^{\mu\nu}$ matrices can be explicitly written as

$$T^{\mu\nu}_{nm,n'm'} = \delta_{nm,n'm'} - \sum_{\alpha\beta\gamma} \hat{\boldsymbol{\rho}}^{\mu\alpha}_{nm} \otimes \hat{\mathbf{D}}^0_{\alpha\beta} \otimes \hat{\boldsymbol{\rho}}^{\beta\gamma}_{n'm'} \hat{\mathbf{F}}^{\gamma\nu}_{n'm'}. \tag{37}$$

After inserting Eqs. (35) and (36) into Eq. (33) we obtain $\hat{\mathbf{D}}^{para}$.

Of course, the set of integral Eq. (33) could be transformed into a set of matrix equations by discretization of the dummy variables, but this procedure is numerically much more demanding, since the functions D^0 and D^{para} are not smooth, i.e., discretization would lead to large matrices.

B. Diamagnetic contribution

After calculating $\hat{\mathbf{D}}^{para}$ we want to include the diamagnetic interaction. With the help of Eq. (15), Eq. (31) becomes

$$\hat{\mathbf{D}}(z,z') = \hat{\mathbf{D}}^{para}(z,z') - \int_{-L}^{0} dz_1 \hat{\mathbf{D}}^{para}(z,z_1) \hat{\mathbf{n}}(z_1) \hat{\mathbf{D}}(z_1,z'), \tag{38}$$

where $\hat{\mathbf{n}}(z)=\frac{e^2}{mc} n(z) \hat{\mathbf{I}}$. Here we did not omit the variables in order to emphasize that, because of the delta function in Eq. (15) we no longer have two convolutions over two dummy variables, but the only remaining dummy variable z_1 appears in both $\hat{\mathbf{D}}^{para}(z,z_1)$ and $\hat{\mathbf{D}}(z_1,z')$. Therefore, this time we cannot use the method from the previous section to transform the set of integral equations into a set of matrix equations, and we have to solve the integral equations numerically, by discretization of the variable z_1.

For *s* polarization the problem is relatively simple since we have just one equation for D_{xx}. However, for *p* polarization we have two sets of two coupled equations, one for D_{yy} and D_{yz} and the other for D_{zy} and D_{zz}.

In order to minimize the numerical effort we can transform these equations, e.g., by separating it into local and

nonlocal contributions. From Eqs. (24) and (32), it is obvious that we can write D_{zz}^{para} in the form

$$D_{zz}^{para}(z,z') = -\frac{4\pi c}{\omega^2}\delta(z-z') + \mathcal{D}_{zz}^{para}(z,z'), \tag{39}$$

where $\mathcal{D}_{zz}^{para}$ is the nonlocal part of D_{zz}^{para}. After inserting that in the set of Eq. (38), with some rearrangements, the complete propagator D_{zz} can be written in the equivalent form

$$D_{zz}(z,z') = -\frac{4\pi c}{\epsilon(z)\omega^2}\delta(z-z') + \mathcal{D}_{zz}(z,z'), \tag{40}$$

where $\mathcal{D}_{zz}$ is the nonlocal part of D_{zz}. Here we introduced the local dielectric function

$$\epsilon(z) = 1 - \frac{\omega_p^2(z)}{\omega^2}$$

and defined $\omega_p^2(z) = \frac{4\pi n(z)e^2}{m}$ as the local plasma frequency.

Occurence of the local dielectric function $\epsilon(z)$ at this point might seem strange, but it is in accordance with the classical theory where dielectric function $\epsilon(\omega)$ appears in the denominator. Even though the classical dielectric function is not a function of z, it is actually position dependent since it is equal to $\epsilon(\omega)$ inside the slab and equal to one outside the slab. This limit can be obtained from our theory by using a rectangular electron-density profile

$$n(z) = n^+\theta(z+L-\Delta)\theta(-z-\Delta) \tag{41}$$

instead of the Kohn-Sham LDA electron density, which correspond to the classical description of the slab.

Using Eqs. (39) and (40) we can transform Eq. (38) into

$$\int_{-L}^{0} dz_1[\hat{\epsilon}(z_1)\hat{\boldsymbol{\delta}}(z-z_1) + \hat{\mathcal{D}}_{para}(z,z_1)\hat{\mathbf{n}}(z_1)]\hat{\mathcal{D}}(z_1,z') = \hat{\mathcal{D}}_{para}(z,z')\hat{\epsilon}^{-1}(z'), \tag{42}$$

where we introduced $\hat{\boldsymbol{\delta}}(z-z') = \delta(z-z')\hat{\mathbf{I}}$,

$$\hat{\epsilon}(z) = \begin{bmatrix} 1 & 0 & 0 \\ 0 & 1 & 0 \\ 0 & 0 & \epsilon(z) \end{bmatrix},$$

$$\hat{\mathcal{D}}_{para}(z,z') = \begin{bmatrix} D_{xx}^{para}(z,z') & 0 & 0 \\ 0 & D_{yy}^{para}(z,z') & D_{yz}^{para}(z,z') \\ 0 & D_{zy}^{para}(z,z') & \mathcal{D}_{zz}^{para}(z,z') \end{bmatrix},$$

and

$$\hat{\mathcal{D}}(z,z') = \begin{bmatrix} D_{xx}(z,z') & 0 & 0 \\ 0 & D_{yy}(z,z') & D_{yz}(z,z') \\ 0 & D_{zy}(z,z') & \mathcal{D}_{zz}(z,z') \end{bmatrix}.$$

Equation (42) is again a set of integral equations, one for s polarization, giving us D_{xx}, plus two sets of two coupled integral equations for p polarization, one for D_{yy} and D_{yz} and the other for D_{zy} and D_{zz}. These equations can now be solved by matrix inversion in real space to give us the complete propagator $\hat{\mathbf{D}}$.

This propagator formalism enables the investigation of various processes, e.g., calculations of the corresponding Feynman diagrams, where both retardation effects and quantum-mechanical description of electronic transitions are important. For example, if we want to study the response to the electromagnetic field at frequencies matching one of the interband transitions in the metallic slab (in the lower ultraviolet range), we can show that the paramagnetic response will dominate, and it will be sufficient to solve the Eq. (33). On the other hand, in the infrared frequency range (below the interband transition energies) diamagnetic response dominates and it will be well described by Eq. (42) with $\hat{\mathbf{D}}^{para}$ replaced by $\hat{\mathbf{D}}^0$. However, in the intermediate region (visible light) both effects are important and strongly influence each other, so in that region we have to solve the complete Eq. (42).

In Sec. V we show that for frequencies $\omega > \omega_p$, i.e., above the frequency of interband transitions (higher part of the ultraviolet frequency range) unexpectedly, both mechanisms are important for the proper description of enhanced radiation produced by the dipole placed inside the metallic slab. We also show that the dielectric theory model, which treats the metallic slab as a dielectric medium with the local dielectric function $\epsilon(\omega)$, corresponds to the solution of Eq. (42) where again $\hat{\mathbf{D}}^{para}$ is replaced by $\hat{\mathbf{D}}^0$ and the dielectric function $\epsilon(z)$ is calculated using a rectangular electron-density profile Eq. (41) instead of the LDA density profile $n(z)$.

C. Formal inclusion of metallic band-structure effects

Our approach can be extended to include the band structure, i.e., more realistic description of metallic crystal structure in rather straightforward manner. Quantities such as Π^{para}, Π^{dia}, and Π^{para} now become matrices with respect to the reciprocal lattice vectors $\mathbf{G}$ in the direction parallel to the surface. For example, matrix elements of the paramagnetic self-energy part become

$$\Pi_{\mu\nu,\mathbf{GG}'}^{para}(\mathbf{Q},\omega,z,z') = -\frac{1}{c}\frac{1}{S}\sum_{\mathbf{K}}^{SBZ}\sum_{i,j}\sum_{n,m}\frac{f_{i,n}(\mathbf{K}) - f_{j,m}(\mathbf{K}+\mathbf{Q})}{\hbar(\omega+i\eta) + E_{i,n}(\mathbf{K}) - E_{j,m}(\mathbf{K}+\mathbf{Q})} \times \langle \mathbf{q}+\mathbf{G}|j_{(i,n,\mathbf{K})\to(j,m,\mathbf{K}+\mathbf{Q})}^{\mu}\rangle\langle j_{(i,n,\mathbf{K})\to(j,m,\mathbf{K}+\mathbf{Q})}^{\nu}|\mathbf{q}+\mathbf{G}'\rangle,$$

where $\mathbf{K}$ is limited to first surface Brillouin zone, sums i, j are over the bands in direction parallel to the surface, and sums n, m are over discrete states in direction perpendicular to the surface. Matrix elements are calculated by integration over a two-dimensional unit cell, and S is the normalization area. Currents producing transitions between Bloch states $u_{i,\mathbf{K}}$ and $u_{j,\mathbf{K}+\mathbf{Q}}$ in the parallel direction and simultaneously between ϕ_n and ϕ_m states in the perpendicular direction are explicitly given by

$$j_{(i,n,\mathbf{K})\to(j,m,\mathbf{K}+\mathbf{Q})}^{\mu} = \frac{e\hbar}{2im}\{\phi_n u_{i,\mathbf{K}}^*\nabla_\mu\phi_m u_{j,\mathbf{K}+\mathbf{Q}} - (\nabla_\mu\phi_n u_{i,\mathbf{K}}^*)\phi_m u_{j,\mathbf{K}+\mathbf{Q}}\}.$$

Matrices of the diamagnetic self-energy part and free-photon propagator become

$$\Pi^{dia}_{\mu\nu,\mathbf{GG}'}(z) = -\frac{e^2}{mc}\rho(\mathbf{G}-\mathbf{G}',z)\delta_{\mu\nu}. \tag{43}$$

and

$$D^0_{\mu\nu,\mathbf{GG}'}(\mathbf{Q},\omega,z,z') = D^0_{\mu\nu}(\mathbf{Q}+\mathbf{G},\omega,z,z')\delta_{\mathbf{GG}'}, \tag{44}$$

where $D^0_{\mu\nu}$ is explicitly given by Eqs. (22)–(25). After calculating all the matrices, the complete propagator can be formally obtained by solving the Dyson equation of the form

$$\hat{\mathbf{D}}_{\mathbf{GG}'} = \hat{\mathbf{D}}^0_{\mathbf{GG}'} + \sum_{\mathbf{G}_1\mathbf{G}_2} \hat{\mathbf{D}}^0_{\mathbf{GG}_1} \otimes [\hat{\mathbf{\Pi}}^{dia}_{\mathbf{G}_1\mathbf{G}_2} + \hat{\mathbf{\Pi}}^{para}_{\mathbf{G}_1\mathbf{G}_2}] \otimes \hat{\mathbf{D}}_{\mathbf{G}_2\mathbf{G}'}. \tag{45}$$

Numerical solution of this equation could be extremely complex. Solving the matrix equation in z direction alone is very complicated, and here in addition to that we have to perform matrix inversion in $\mathbf{G}$ space. Nevertheless, there are some possibilities to simplify this calculation dramatically without losing the physical information originating from the band structure. Namely, as demonstrated in Refs. 32 and 44, for simple metals and in the long-wavelength limit local field effects (higher $\mathbf{G}$ contributions in the free-response function) are almost unimportant and it is sufficient to keep only the $\mathbf{G}=0,\mathbf{G}'=0$ contribution. In that case solving Eq. (45) reduces to the previously presented method with just one difference; now all band structure effects are included in $\hat{\mathbf{\Pi}}^{para}_{\mathbf{G}=0,\ \mathbf{G}'=\mathbf{0}}$ through Bloch wave functions $\phi_n u_{i,\mathbf{K}}$ and energies $E_{n,i,\mathbf{K}}$. Further simplification could be retaining the two-dimensional translational invariance in the direction parallel to the surface and using some one-dimensional model pseudopotential in the perpendicular direction.[45]

V. RESULTS

A. Calculation of the polariton spectra

In the numerical calculation of the polariton spectra we use $e^2=m=\hbar=c=1$ system of units. It means that the unit for measuring distance is Bohr radius ($a_0=\frac{\hbar^2}{me^2}$), unit for wave vectors is inverse Bohr radius and unit for energy and frequency is Hartree $Ha=\frac{e^2}{a_0}$. Also the wave vector $k_\perp$ which appears in the free-space propagator $D^0_{\mu\nu}$ is

$$k_\perp = \sqrt{\gamma^2\omega^2 - Q^2},$$

where $\gamma=\frac{e^2}{\hbar c}\approx\frac{1}{137}$ is the fine-structure constant. Bulk and surface plasma frequencies are 0.61(16.7) and 0.43(11.8) Ha(eV), respectively. For the numerical integration of the matrix elements [Eq. (37)] and solution of the integral equation [Eq. (42)] we used Gauss-Legendre method and sampling the slab region of width $34a_0$ by 80 points.

Knowing $D_{\mu\nu}$ one can easily calculate spectra $A_{\mu\nu}$ of radiative and nonradiative polariton modes, i.e., electromagnetic fields coupled to the electronic excitations in a metallic slab in a standard way

$$A_{\mu\nu}(Q,\omega,z,z') = \frac{1}{\pi}|\mathrm{Im}\ D_{\mu\nu}(Q,\omega,z,z')|, \tag{46}$$

where z' and z define the positions of perturbing current and observed fields in directions ν and μ, respectively. Or, we can get a better physical meaning by considering the induced electrical field $E_\mu(Q,\omega,z)$ as response to the external current with the Q-component $j^{ext}_\nu(Q,\omega,z_1)$ (see Appendix B)

$$E_\mu(Q,\omega,z) = i\frac{\omega}{c}\int dz' D_{\mu\nu}(Q,\omega,z,z')j^{ext}_\nu(Q,\omega,z'). \tag{47}$$

Obviously, Q and ω are conserved, and polarization μ is determined by the symmetry properties of $D_{\mu\nu}$. In real-space Eq. (47) corresponds to

$$E_\mu(\mathbf{r},\omega) = i\frac{\omega}{c}\int d\mathbf{r}' D_{\mu\nu}(\mathbf{r},\mathbf{r}',\omega)j^{ext}_\nu(\mathbf{r}',\omega) \tag{48}$$

and the response to the point dipole

$$j^{ext}_\nu(\omega,\mathbf{r}') = -i\omega\delta(\mathbf{r}_1-\mathbf{r}')P_\nu \tag{49}$$

would contain all Q components, as will be the case in Sec. V B. We shall consider local response ($z=z'$) to the perturbing current with the Q-component $j^{ext}_\nu(Q,\omega,z)$ placed at distance z from the metallic surface, and calculate the diagonal terms

$$A_\mu(Q,\omega,z) = \frac{1}{\pi}|\mathrm{Im}\ D_{\mu\mu}(Q,\omega,z,z)|. \tag{50}$$

From Eqs. (48) and (49) we find the proportionality

$$E_\mu(Q,\omega,z) = \frac{\omega^2}{c}D_{\mu\mu}(Q,\omega,z,z)P_\mu, \tag{51}$$

so that we can analyze polariton spectra by plotting

$$\frac{1}{\pi}|\mathrm{Im}\ E_\mu(Q,\omega,z)| = \frac{\omega^2}{c}A_\mu(Q,\omega,z) \tag{52}$$

for $P_\mu=1$. Obviously, $A_x(Q,\omega,z)$ corresponds to spectra of s-polarized polaritons whereas $A_y(Q,\omega,z)$ and $A_z(Q,\omega,z)$ correspond to the spectra of p-polarized polaritons.

As an example, we present spectra for the jellium slab with $r_s=2$ and thickness $d=10a_0$. Most convenient choice for the distance where the electron density practically vanishes turns out to be $\Delta=12a_0$, meaning the total slab thickness is $L=34a_0$.

Figure 5 shows $\frac{\omega^2}{c}A_y$ outside and inside the metallic slab. For $\omega<Qc$, where modes with electric field localized in the surface region are possible, the spectra show sharp resonant peaks belonging to two surface polaritons. The one denoted as $SP1$ is even, while $SP2$ is odd, which refers to the symmetry of the polarization fields with respect to the slab. For $Q=0.002a_0^{-1}$ and $0.003a_0^{-1}$ odd polariton is not visible because it overlaps with radiative modes appearing above $\omega=Qc$. For $Q=0.004a_0^{-1}$ and $0005a_0^{-1}$ it can be distinguished but the corresponding peak is still very small. Finite spectral weight in $\omega>Qc$ region belongs to the continuum of radiative modes with electric field having oscillatory character in z direction.

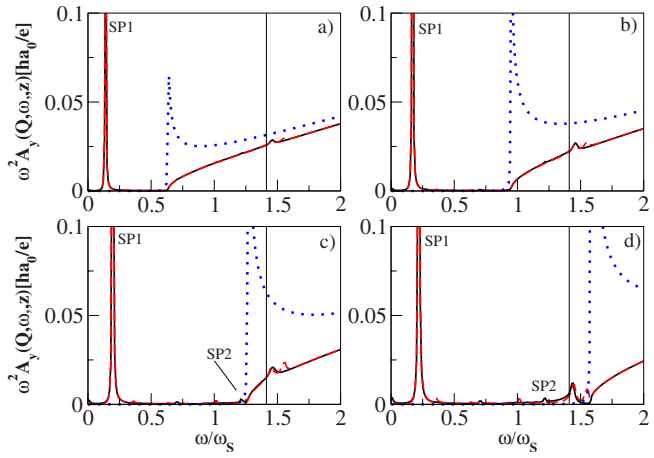

FIG. 5. (Color online). Spectra of p-polarized polaritons $\frac{\omega^2}{c}A_y$ for $z=0a_0$ (black-full line) and $z=-19a_0$ (red dashed line). Blue (dotted) lines show spectra of s-polarized polaritons $\frac{\omega^2}{c}A_x$. Wave vector Q are: (a) $0.002a_0^{-1}$; (b) $0.003a_0^{-1}$; (c) $0.004a_0^{-1}$; and (d) $0.005a_0^{-1}$. Thin vertical line represents the position of the bulk plasma frequency ω_p.

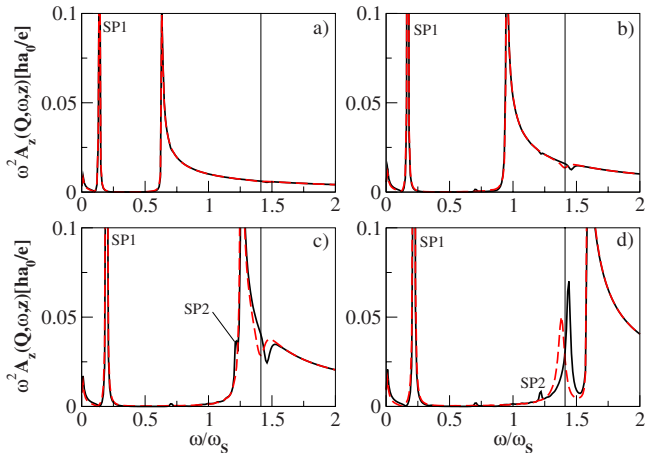

FIG. 6. (Color online). Spectra of p-polarized polaritons $\frac{\omega^2}{c}A_z$ for $z=0a_0$. Black (full) lines show complete spectra. Red (dashed) lines show diamagnetic contributions to the spectra. Wave vectors Q are: (a) $0.002a_0^{-1}$; (b) $0.003a_0^{-1}$; (c) $0.004a_0^{-1}$; and (d) $0.005a_0^{-1}$. Thin vertical line represents the position of the bulk plasma frequency ω_p.

Spectra $\frac{\omega^2}{c}A_y$ for points z outside the slab, at $z=0$ (black-full lines), and inside the slab at $z=-19a_0$ (red-dashed lines) are slightly different. Inside the slab and for larger Q the spectra show low-intensity peaks corresponding to intersubband transitions, i.e., transitions from occupied to unoccupied discrete states without parallel momentum transfer. Blue-dotted lines in Fig. 5 show $\frac{\omega^2}{c}A_x$, the intensity of s-polarized electromagnetic field for various wave vectors and for the point placed outside ($z=0a_0$) the metallic slab. In the $\omega<Qc$ region s-polarized response is very weak and does not show any resonant peaks. This means that in this region there is no polarization mechanism to propagate x-polarized electric field (as predicted by the classical theory[39]). Inside the metallic slab ($z=-19a_0$) spectra for s polarization are almost exactly the same as outside ($z=0a_0$), which means that s-polarized perturbation very weakly polarizes the metallic slab regardless of its position.

The spectra $\frac{\omega^2}{c}A_z$ near the metallic slab surface ($z=0a_0$) are shown by black-full lines in Fig. 6. Red-dashed line shows the diamagnetic contribution only, i.e., spectra obtained from Eq. (42) with D^{para} replaced by D^0. Very small differences between these spectra confirm that the contribution of the interband electron-hole transitions (appearing in the current-current response function) to the complete spectra outside the metal is negligible. Moreover, if we use rectangular electron density instead of the Kohn-Sham density (shown in Fig. 1), we obtain the diamagnetic spectra identical to the spectra obtained by solving the Maxwell equations for the perturbation placed near the metallic slab described by some local dielectric function $\epsilon(\omega)$

$$E_z(Q,\omega,z)=\frac{2\pi iQ^2}{k_\perp}\{1+r_p^{slab}e^{-2ik_\perp z}\},$$

where $r_p^{slab}=\frac{r_p}{D_p}(1-e^{2ik'_\perp d})$ is the reflection coefficient for p-polarized electromagnetic-wave incident on the metallic-slab surface, r_p is the reflection coefficient for p-polarized wave incident to vacuum/metal interface, $D_p=1-r_p^2e^{2ik'_\perp d}$, and $k'_\perp=\sqrt{\epsilon(\omega)\frac{\omega^2}{c^2}-Q^2}$. Frequencies of surface polaritons for various Q calculated by using condition $r_p^{slab}=\infty$ correspond to the positions of resonant peaks $SP1$ and $SP2$ in Fig. 6. This means that including only the diamagnetic response is sufficient for the description of electromagnetic excitation spectra outside the metal. Therefore, as we can see from Eq. (42), the only quantity needed to calculate such spectra is the ground-state electronic density. This also means that including only the diamagnetic response in construction of the electromagnetic propagator is some kind of long-range extension of the local density approximation which may be very useful in studying, e.g., van der Waals interaction and similar phenomena.

For points z, z' inside the metallic slab the situation is very different. Black-full lines in Figs. 7 show complete spectra $\frac{\omega^2}{c}A_y$ of z-polarized electromagnetic field for $z=-19.0a_0$. We can see two very intense peaks—several hundred times stronger then the ones shown on Fig. 6, for the field outside the metal. One is located around the bulk plasmon frequency and the other $0.1\omega_S$ above it. To determine the origin of these peaks we separate complete spectra into diamagnetic and paramagnetic contributions. Blue-dashed lines show the paramagnetic contribution obtained by solving Eq. (33), describing the situation when only current-current contribution to photon self-energy is included. We can see sharp peaks corresponding to interband excitations. On the other hand red-dotted lines represent the spectra when only diamagnetic response is included. We recognize the intense peaks positioned at bulk plasmon frequency ω_p. The existence of such peaks is obvious from Eq. (42), since the function $\epsilon^{-1}(\omega,z')$ (appearing on the rhs) inside the metal has a pole at $\omega\approx\omega_p$. This can be proved by solving the Maxwell equation for the perturbation placed inside the metal and getting

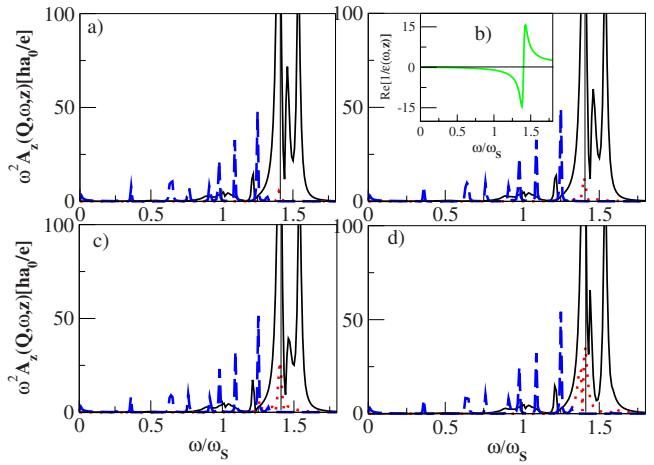

FIG. 7. (Color online). Spectra of p-polarized polaritons $\frac{\omega^2}{c}A_z$ for $z=-19a_0$. Black (full) lines—complete spectra, red (dotted) lines—diamagnetic contribution, and blue (dashed) lines—paramagnetic contribution. Green line (inserted picture)—the screening strength $[\epsilon^{-1}(\omega,z)]$ inside the metallic slab ($z=-19a_0$). Wave vectors Q are: (a) $0.002a_0^{-1}$; (b) $0.003a_0^{-1}$; (c) $0.004a_0^{-1}$; and (d) $0.005a_0^{-1}$. Thin vertical line represents the position of the bulk plasma frequency ω_p.

$$E_z(Q,\omega,z)=\frac{2\pi iQ^2}{\epsilon(\omega)k'_\perp D_p}\{1-r_p[e^{2ik'_\perp z}+e^{-2ik'_\perp(z-d)}]+r_p^2e^{2ik'_\perp d}\}. \tag{53}$$

The quantity $\epsilon(\omega)k'_\perp$ in the denominator is responsible for two resonant peaks at $\omega=\omega_p$ and $\omega=\sqrt{\omega_p^2+Q^2c^2}$ which overlap for $Q\approx 0$. Moreover, the whole spectra obtained from Eq. (53) are in excellent agreement with the red spectra in Fig. 7. However, the full spectrum is more intense and there is a peak above ω_p.

Possible explanation of such behavior can be as follows. When diamagnetic polarizability is neglected, z-polarized field inside the metal induces interband electron-hole transitions which produce current in z direction (which, for $Q\approx 0$, is constant along the whole surface). That current couples to p-polarized electromagnetic field to create exciton-like fluctuations, i.e., sharp peaks shown in blue-dashed lines. After the diamagnetic contribution is included the whole spectra formally can be calculated from Eq. (31), which can be symbolically written as

$$D=\frac{D^{para}}{1-D^{para}\Pi^{dia}}.$$

So the diamagnetic contribution to the spectra leads to the screening of the paramagnetic contribution and the frequency shifts in the spectra. This can also be seen more directly from Eq. (42) where again the factor $\epsilon^{-1}(\omega,z')$ on the rhs (plotted as a green line in Fig. 7) indicates that the screening of the paramagnetic field is the most efficient in the region $\omega<\omega_p$, which explains the strong reduction in the exciton intensity in that region. On the other hand, in region $\omega>\omega_p$ the screening is inverted $(1/\epsilon>1)$, so this is the region where excitonic weight in the complete spectra conserves their normalization. Obviously, excitons (blue-dashed line) and bulk plasmon-polaritons (red-dotted line) strongly hybridize forming the new spectra (black line).

B. Enhancement of the electric field near surface

Enhancement of the radiating field produced by an oscillating dipole when the dipole is placed near a metallic surface is a well-known phenomenon.[4,6,31] We can use our approach to calculate and study this enhancement, both outside and inside the slab. The current produced by a point dipole P_ν placed at point $\mathbf{r}'=(0,0,z')$ is

$$j_\nu^{ext}(\mathbf{r},\omega)=-i\omega P_\nu^0\delta(\boldsymbol{\rho})\delta(z-z'). \tag{54}$$

Electric field at point $\mathbf{r}=(\boldsymbol{\rho},z)$ produced by that current can be obtained from Eq. (B1), with $D_{\mu\nu}$ instead of $D^0_{\mu\nu}$

$$E_\mu(\mathbf{r},\omega)=\frac{\omega^2}{c}D_{\mu\nu}(\boldsymbol{\rho},z,z',\omega)P_\nu. \tag{55}$$

This can be Fourier transformed as

$$E_\mu(\mathbf{r},\omega)=\frac{\omega^2}{c}\int\frac{QdQ}{2\pi}J_0(Q\rho)D_{\mu\nu}(Q,\omega,z,z')P_\nu, \tag{56}$$

where J_0 is the zero-order Bessel function. In the following we assume that $\boldsymbol{\rho}=0$ and that the dipole is z polarized, so the z-oriented (incident and reflected) field becomes

$$E_z(\boldsymbol{\rho}=0,z,\omega)=\frac{\omega^2}{c}\int_0^\infty\frac{QdQ}{2\pi}D_{zz}(Q,\omega,z,z')P_z. \tag{57}$$

When z' enters the region of electron density and $z>0$, the polariton propagator has the form[39]

$$D_{zz}(Q,\omega,z,z')=e^{ik_\perp z}D_{zz}(Q,\omega,0,z').$$

and complete electric field is then

$$E_z(\boldsymbol{\rho}=0,z,\omega)=\frac{\omega^2P_z}{2\pi c}\int_0^\infty dQQe^{ik_\perp z}D_{zz}(Q,\omega,0,z').$$

In the region $Q<\frac{\omega}{c}$ the modes are radiative and reach far into vacuum, but for $Q>\frac{\omega}{c}$ and $\omega<\omega_p$ the dipole can also couple to the localized surface polaritons which produce fields decaying in the region $z\leq Q^{-1}$. Since we want to investigate the enhancement of the radiating field far away from the metallic surface we choose $z=1000a_0$. To avoid plasma and exciton resonances shown in Fig. 7 we choose $\omega>\omega_p$. It is useful to define field-enhancement parameter as the ratio of electric field at point z produced by the dipole placed at arbitrary point z' and the dipole placed just outside the metal, at $z'=0$

$$\Gamma_z(\omega,z,z')=\frac{\mathrm{Re}\,E_z(\omega,z,z')}{\mathrm{Re}\,E_z(\omega,z,0)}.$$

Black-full lines in Fig. 8 show the field enhancement parameter as a function of the dipole position. When the dipole frequency $\omega=1.5\omega_S$ is slightly above the plasma frequency [Fig. 8(a)], and the dipole is placed inside the slab ($z'=-14a_0$) radiating field is around twenty times stronger com-

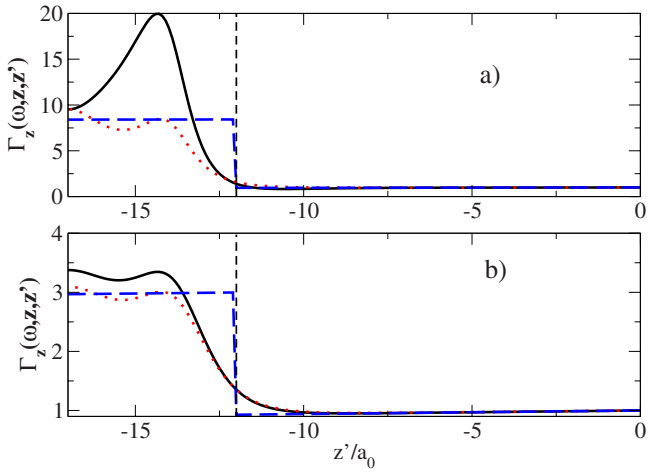

FIG. 8. (Color online). Black (full) lines show the radiating electric field enhancement as function of oscillating dipole position z'. Red (dotted) lines show enhanced field when only diamagnetic response is included. Blue (dashed) lines show the enhancement obtained for rectangular density profile or by solving the Maxwell equations. Observer position is $z=1000a_0$. Oscillating dipole frequencies are (a) $\omega=1.5\omega_p$ and (b) $1.7\omega_p$. Dashed lines denote the position of the jellium edge.

pared to the situation when the dipole is placed outside of the slab ($z'=0a_0$). For a higher dipole frequency $\omega=1.7\omega_S$ [Fig. 8(b)] the enhancement field parameter is only around three.

Red-dotted lines in Fig. 8 show the field enhancement parameter when only the diamagnetic polarizability is included. If we perform the same calculation, but starting from the rectangular electron density (instead of Kohn-Sham density), we obtain the result shown by the blue-dashed line. This result corresponds to the classical result obtained by solving the Maxwell equations with the slab represented by a dielectric medium described by the dielectric function $\epsilon=1-\frac{\omega_p^2}{\omega^2}$, of the same thickness as our jellium. Comparing these results with the density profiles in Fig. 1 it is obvious that the enhancement follows the density distribution. We see that for $\omega=1.5\omega_p$ the enhancement is reduced almost by the factor two. This effect can also be observed in Fig. 7 where the strong resonant peak at $\omega\approx1.5\omega_p$ is missing when only diamagnetic response is included. For $\omega=1.7\omega_p$ enhancement is not that much reduced. Enhancement in the surface region $z'\approx-12a_0$ is weak, and does not depend on whether the paramagnetic response is included or not.

This shows that including the current-current response which contains interband electron-hole transitions is very important. On the other hand, if only diamagnetic polarizability is included the enhanced field produced by dipole placed inside the metal is modified and reduced. So two polarization mechanisms work together to produce the enhancement even above the resonant features in the spectra (when only virtual processes contribute) and at large distances when one expects that only the classical effects are important.

The validity of all the above results can also be examined by comparing the spectra in the nonretarded limit [$c\to\infty$ in Eq. (52)] with the spectra obtained by using the propagator of screened Coulomb interaction $W(Q,\omega,z,z')$.[37,38,46,47] Namely, we confirmed that $D_{\mu\nu}$ in nonretarded limit can be related to W as

$$\lim_{c\to\infty}\frac{\omega^2}{c}D_{\mu\nu}(Q,\omega,z,z') = -\left[i\mathbf{Q}+\mathbf{z}\frac{\partial}{\partial z}\right]_\mu\left[-i\mathbf{Q}+\mathbf{z}\frac{\partial}{\partial z'}\right]_\nu W(Q,\omega,z,z').$$

VI. CONCLUSION

In this paper we developed the quantum-mechanical formalism which enables calculation of the electromagnetic-field propagator in the presence of a thin metallic slab. The formalism is based on diagrammatic approach using DFT within LDA as a starting point to describe electronic excitations. The propagator is obtained by numerical solution of the Dyson equation, which is given in terms of a free-photon Green's function and photon self-energy (i.e., slab conductivity tensor), which can both be calculated analytically, as shown in the appendices, except for the electron wave functions that are obtained numerically as solutions of the Kohn-Sham equations. We derived long-wavelength limit of the response function and the quasistatic limit of the free-photon propagator, and compared them with previous results.

To minimize the numerical effort we took advantage of the symmetry of the problem and divided the equations for s and p polarizations, which are shown to be independent and therefore can be treated separately. We also divided the response into diamagnetic (local) and paramagnetic (nonlocal) parts, and treated each of them separately, since local and nonlocal problems are incompatible numerically and require completely different procedure. Even though from the numerical point of view these types of response were treated separately, our formalism enabled taking both mechanisms into account as well as their mutual influence.

Using this formalism we calculated spectra of electromagnetic excitations produced by an oscillating perturbation placed in the vicinity or inside a metallic slab. We showed that spectra in region outside the metal for frequencies $\omega<Qc$ have two sharp peaks corresponding to two surface polaritons, and for frequencies $\omega>Qc$ there is a continuum of radiative modes. Also, the spectra outside the metal are almost independent of the paramagnetic part of the response function $\Pi_{\mu\nu}$. This means that outside of the metal diamagnetic response is dominant and therefore the spectra corresponds to the classical spectra obtained by solving the Maxwell equations and using local dielectric function.[39]

On the other hand, inside the metal spectra are very different since both polarization mechanisms are very important, and they strongly influence each other. Paramagnetic response contributes with intense sharp peaks corresponding to the blueshifted interband transition. Diamagnetic response contributes to the peaks which represent longitudinal (bulk) modes, since they are located around bulk plasma frequency $\omega\approx\omega_p$, i.e., at frequencies for which local dielectric function $\epsilon(\omega,z)$ is equal to zero. When both polarization mechanisms are included the spectra are strongly modified.

We compared our results with the classical results and showed that correspondence can be obtained by replacing

our nonlocal dielectric function with the classical dielectric function, since in both cases the dielectric function is directly related to the electron density.

Finally, we investigated the enhancement of the electric field produced by a point dipole placed inside metallic slab, and showed that it changes significantly when the paramagnetic contribution is taken into account. We also demonstrated its dependence on the electronic-density profile, which was discovered long time ago.[4,6] This confirms that the microscopic formulation of $D_{\mu\nu}$ is necessary for an accurate description of the relevant experiments. In the future, results presented here could be improved by using *ab initio* methods. Systems which could be investigated first are simple metal (such as lithium, beryllium, and boron) monolayers,[36] and the first step of this procedure was briefly formulated in this paper.

ACKNOWLEDGMENTS

V.D., M.S., and L.M. are grateful to Marin S. Tomaš for useful discussions and critical reading of the manuscript, and to Ivan Kupčić for several useful suggestions.

APPENDIX A: CURRENT-CURRENT RESPONSE FUNCTION

1. Self-energy component Π_{yy}^{para}

We start from Eqs. (16) and (17). Since we have chosen vector $\mathbf{Q}$ to be in K_y direction, we shall first calculate Π_{yy}^{para}. With this choice of the coordinate system, the y component of the current producing $n\rightarrow m$ transition is

$$j_{nm}^{y}(2\mathbf{K}+\mathbf{Q},z)=\frac{e\hbar}{2m}(2K_y+Q)\phi_n(z)\phi_m(z). \tag{A1}$$

Expressions (16) and (A1), after some rearrangements, give

$$\Pi_{yy}^{para}(\mathbf{Q},\omega,z,z')=-\frac{e^2\hbar^2}{4m^2c}\sum_{nm} I_{nm}^{yy}(\mathbf{Q},\omega)\phi_n(z)\phi_m(z)\phi_n(z')\phi_m(z'),$$

where I_{nm}^{yy} is the following integral over wave vector $\mathbf{K}$

$$I_{nm}^{yy}(\mathbf{Q},\omega)=2\int\frac{d\mathbf{K}}{(2\pi)^2}f_n(\mathbf{K})(2K_y+Q)^2\times\left[\frac{1}{\hbar(\omega+i\eta)+E_n(\mathbf{K})-E_m(\mathbf{K}+\mathbf{Q})}+\frac{1}{\hbar(\omega+i\eta)+E_m(\mathbf{K}+\mathbf{Q})-E_n(\mathbf{K})}\right].$$

The $\mathbf{K}$ integration can be performed as follows: after introducing the polar coordinate system (Fig. 4)

$$K_x=K\sin\theta,\quad K_y=K\cos\theta,\quad dK_xdK_y=KdKd\theta$$

and using $T=0$ Fermi-Dirac function

$$f_n(\mathbf{K})=\theta\left(E_F-E_n-\frac{\hbar^2K^2}{2m}\right)=\theta(K_F^n-K)\theta(E_F-E_n),$$

where

$$K_F^n=\sqrt{\frac{2m}{\hbar^2}(E_F-E_n)}$$

we have

$$I_{nm}^{yy}(Q,\omega)=\frac{2}{(2\pi)^2}\theta(E_F-E_n)\int_0^{K_F^n}KdK\int_0^{2\pi}d\theta(2K\cos\theta+Q)^2\times\left[\frac{1}{\hbar(\omega+i\eta)+E_n-E_m-\frac{\hbar^2Q^2}{2m}-\frac{\hbar^2KQ}{m}\cos\theta}+\frac{1}{\hbar(\omega+i\eta)+E_m-E_n+\frac{\hbar^2Q^2}{2m}+\frac{\hbar^2KQ}{m}\cos\theta}\right].$$

The integration over θ can be expressed as a sum in terms of the standard integrals

$$\int_0^{2\pi}d\theta\frac{\cos^n\theta}{a+b\cos\theta} \tag{A2}$$

with $n=0,1,2$. Substituting $z=e^{i\theta}$ and using theorem of residues these integrals can be solved analytically.

The K integration is trivial, leading to

$$\Pi_{yy}^{para}(\mathbf{Q},\omega,z,z')=\sum_{n=1}^{N_{occ}}\sum_{m=1}^{\infty}F_{nm}^{yy}(Q,\omega)\phi_n(z)\phi_m(z)\phi_n(z')\phi_m(z'), \tag{A3}$$

where N_{occ} is the number of occupied perpendicular levels, and

$$F_{nm}^{xx}(Q,\omega)=\frac{m^2e^2}{\pi c\hbar^6Q^4}\Big\{sgn[a_{nm}(Q,\omega)]\sqrt{A_{nm}(Q,\omega)}[\hbar(\omega+i\eta)+E_n-E_m]^2-sgn[b_{nm}(Q,\omega)]\sqrt{B_{nm}(Q,\omega)}\times[\hbar(\omega+i\eta)+E_m-E_n]^2+b_{nm}(Q,\omega)[\hbar(\omega+i\eta)+E_m-E_n]^2-a_{nm}(Q,\omega)[\hbar(\omega+i\eta)+E_n-E_m]^2+\left[\frac{\hbar^2QK_F^n}{m}\right]^2\left(E_n-E_m+\frac{\hbar^2Q^2}{2m}\right)\Big\}$$

with

$$A_{nm}(Q,\omega)=[a_{nm}(Q,\omega)]^2-\left(\frac{\hbar^2QK_F^n}{m}\right)^2,$$

$$B_{nm}(Q,\omega)=[b_{nm}(Q,\omega)]^2-\left(\frac{\hbar^2QK_F^n}{m}\right)^2,$$

$$a_{nm}(Q,\omega)=\hbar(\omega+i\eta)+E_n-E_m-\frac{\hbar^2Q^2}{2m},$$

and

$$b_{nm}(Q,\omega)=\hbar(\omega+i\eta)+E_m-E_n+\frac{\hbar^2Q^2}{2m}.$$

2. Self-energy component Π_{xx}^{para}

Since the x component of the current producing $n \to m$ transition is

$$j_{nm}^{x}(2\mathbf{K}+\mathbf{Q},z) = \frac{e\hbar}{m} K_x \phi_n(z)\phi_m(z) \tag{A4}$$

expression (16) now gives

$$\Pi_{xx}^{para}(\mathbf{Q},\omega,z,z') = -\frac{e^2\hbar^2}{m^2 c}\sum_{nm} I_{nm}^{xx}(\mathbf{Q},\omega)\phi_n(z)\phi_m(z)\phi_n(z')\phi_m(z') \tag{A5}$$

with

$$I_{nm}^{xx}(Q,\omega) = \frac{2}{(2\pi)^2}\theta(E_F - E_n)\int_0^{K_F^n} K^3 dK \int_0^{2\pi} d\theta \sin^2\theta \times \left[\frac{1}{\hbar(\omega+i\eta)+E_n-E_m-\frac{\hbar^2Q^2}{2m}-\frac{\hbar^2KQ}{m}\cos\theta} + \frac{1}{\hbar(\omega+i\eta)+E_m-E_n+\frac{\hbar^2Q^2}{2m}+\frac{\hbar^2KQ}{m}\cos\theta}\right].$$

This time only the integrals of type Eq. (A2), where $n=0$ and 2 appear in the angular integration, leading to

$$\Pi_{xx}^{para}(\mathbf{Q},\omega,z,z') = \sum_{n=1}^{N_{occ}}\sum_{m=1}^{\infty} F_{nm}^{xx}(Q,\omega)\phi_n(z)\phi_m(z)\phi_n(z')\phi_m(z'), \tag{A6}$$

where

$$F_{nm}^{yy}(Q,\omega) = -\frac{m^2e^2}{3\pi c\hbar^6 Q^4}\left\{sgn[a_{nm}(Q,\omega)]\sqrt{A_{nm}(Q,\omega)}A_{nm}(Q,\omega) - sgn[b_{nm}(Q,\omega)]\sqrt{B_{nm}(Q,\omega)}B_{nm}(Q,\omega) + [b_{nm}(Q,\omega)]^3 - [a_{nm}(Q,\omega)]^3 + 3\left[\frac{\hbar^2QK_F^n}{m}\right]^2\left(E_n - E_m - \frac{\hbar^2Q^2}{2m}\right)\right\}.$$

3. Self-energy component Π_{zz}^{para}

The perpendicular current associated with the $n \to m$ transition is [see Eq. (17)]

$$j_{nm}^{z}(2\mathbf{K}+\mathbf{Q},z) = \frac{e\hbar}{2im} j_{nm}(z) \tag{A7}$$

with

$$j_{nm}(z) = \phi_n(z)\partial_z\phi_m(z) - \phi_m(z)\partial_z\phi_n(z).$$

This time Eq. (16) gives

$$\Pi_{zz}^{para}(\mathbf{Q},\omega,z,z') = \frac{e^2\hbar^2}{4m^2 c}\sum_{nm} I_{nm}^{zz}(\mathbf{Q},\omega) j_{nm}(z) j_{mn}(z'), \tag{A8}$$

where I^{zz} is

$$I_{nm}^{zz}(Q,\omega) = \frac{2}{(2\pi)^2}\theta(E_F - E_n)\int_0^{K_F^n} K dK \int_0^{2\pi}\left[\frac{d\theta}{\hbar(\omega+i\eta)+E_n-E_m-\frac{\hbar^2Q^2}{2m}-\frac{\hbar^2KQ}{m}\cos\theta} - \frac{d\theta}{\hbar(\omega+i\eta)+E_m-E_n+\frac{\hbar^2Q^2}{2m}+\frac{\hbar^2KQ}{m}\cos\theta}\right].$$

This integral is the simplest one because the only angular integral is of type Eq. (A2), where $n=0$. After integration, taking into account that $j_{mn}=-j_{nm}$, we get

$$\Pi_{zz}^{para}(\mathbf{Q},\omega,z,z') = \sum_{n=1}^{N_{occ}} \sum_{m=1}^{\infty} F_{nm}^{zz}(Q,\omega) j_{nm}(z) j_{nm}(z'), \tag{A9}$$

where

$$F_{nm}^{zz}(Q,\omega) = \frac{e^2}{4\pi c\hbar^2 Q^2}\Bigg\{ sgn[a_{nm}(Q,\omega)]\sqrt{A_{nm}(Q,\omega)} - sgn[b_{nm}(Q,\omega)]\sqrt{B_{nm}(Q,\omega)} + 2\left(E_m - E_n + \frac{\hbar^2 Q^2}{2m}\right)\Bigg\}$$

4. Self-energy components Π_{yz}^{para} and Π_{zy}^{para}

After inserting the currents Eqs. (A1) and (A7) in Eq. (16), we get

$$\Pi_{yz}^{para}(\mathbf{Q},\omega,z,z') = \frac{ie^2\hbar^2}{4m^2 c}\sum_{nm} I_{nm}^{yz}(Q)\phi_n(z)\phi_m(z) j_{mn}(z'), \tag{A10}$$

$$\Pi_{zy}^{para}(\mathbf{Q},\omega,z,z') = \frac{ie^2\hbar^2}{4m^2 c}\sum_{nm} I_{nm}^{yz}(Q) j_{nm}(z)\phi_n(z')\phi_m(z'). \tag{A11}$$

K integral is the same in both cases and has the form

$$I_{nm}^{yz}(Q) = \frac{2}{(2\pi)^2}\theta(E_F - E_n)\int_0^{K_F^n} KdK \int_0^{2\pi} d\theta(2K\cos\theta + Q) \times\left[\frac{1}{\hbar(\omega + i\eta) + E_n - E_m - \frac{\hbar^2 Q^2}{2m} - \frac{\hbar^2 KQ}{m}\cos\theta} - \frac{1}{\hbar(\omega + i\eta) + E_m - E_n + \frac{\hbar^2 Q^2}{2m} + \frac{\hbar^2 KQ}{m}\cos\theta}\right].$$

After integration, using Eq. (A2), where $n=0$ and 1, and taking into account $j_{mn}=-j_{nm}$, we get

$$\Pi_{yz}^{para}(\mathbf{Q},\omega,z,z') = \sum_{n=1}^{N_{occ}} \sum_{m=1}^{\infty} F_{nm}^{yz}(Q,\omega)\phi_n(z)\phi_m(z) j_{mn}(z'), \tag{A12}$$

$$\Pi_{zy}^{para}(\mathbf{Q},\omega,z,z') = \sum_{n=1}^{N_{occ}} \sum_{m=1}^{\infty} F_{nm}^{zy}(Q,\omega) j_{nm}(z)\phi_n(z')\phi_m(z'), \tag{A13}$$

where

$$F_{nm}^{yz}(Q,\omega) = -F_{nm}^{zy}(Q,\omega) = i\frac{e^2 m}{2\pi c\hbar^4 Q^3}\Bigg\{ sgn[a_{nm}(Q,\omega)]\sqrt{A_{nm}(Q,\omega)} \times[\hbar(\omega + i\eta) + E_n - E_m] + sgn[b_{nm}(Q,\omega)] \times\sqrt{B_{nm}(Q,\omega)}[\hbar(\omega + i\eta) + E_m - E_n] - 2\hbar^2(\omega + i\eta)^2 - 2(E_m - E_n)\left[E_m - E_n + \frac{\hbar^2 Q^2}{2m}\right] + \left[\frac{\hbar^2 QK_F^n}{m}\right]^2\Bigg\}.$$

There is no need to analyze in detail the other four components because it is easy to see that they are all equal to zero. Indeed, since x current

$$j_{nm}^x(2\mathbf{K} + \mathbf{Q}, z) = \frac{e\hbar}{m} K_x \phi_n(z)\phi_m(z)$$

is linear in sin θ, i.e., odd as a function of θ, obviously

$$\Pi_{xy}^{para} = \Pi_{yx}^{para} = \Pi_{xz}^{para} = \Pi_{zx}^{para} = 0.$$

APPENDIX B: FREE-PHOTON PROPAGATOR

In this section we shall derive the free-photon propagator $D_{\mu\nu}^0$ defined in Eq. (8) by connecting it with the electric field $E_\mu(\mathbf{r},\mathbf{r}',\omega)$ at the point $\mathbf{r}$ produced by a point dipole placed at $\mathbf{r}'$, following the procedure presented in Ref. 39. As is well known,[42] the Green's functions (8) coincides with the classical Green's function for the classical Maxwell's equations. The electric field produced by a classical external current distribution $j_\nu(\mathbf{r},\omega)$ is given by

$$E_\mu(\mathbf{r},\omega) = i\frac{\omega}{c}\sum_\nu \int d\mathbf{r}_1 D_{\mu\nu}^0(\mathbf{r},\mathbf{r}_1,\omega) j_\nu(\mathbf{r}_1,\omega). \tag{B1}$$

Suppose that the external current is produced by an oscillating point dipole $\mathbf{P}_0 e^{-i\omega t}$ at point $\mathbf{r}'$, i.e.,

$$j_\nu(\mathbf{r}_1,\omega) = -i\omega P_0^\nu \delta(\mathbf{r}_1 - \mathbf{r}'). \tag{B2}$$

After inserting this in Eq. (B1) and Fourier transforming in the direction parallel to the surface, we get the expression for electric field in terms of $D_{\mu\nu}^0$

$$E_\mu(Q,\omega,z,z') = \frac{\omega^2}{c} D_{\mu\nu}^0(Q,\omega,z,z') P_0^\nu. \tag{B3}$$

On the other hand, the electric field of the dipole can be obtained directly by solving Maxwell's equations. After combining the Faraday and Ampere laws we get[39]

$$\left\{\nabla\times\nabla\times - \frac{\omega^2}{c^2}\hat{\mathbf{I}}\right\}\mathbf{E}(\mathbf{r},\mathbf{r}',\omega) = 4\pi\frac{\omega^2}{c^2}\delta(\mathbf{r} - \mathbf{r}')\mathbf{P}_0, \tag{B4}$$

where $\hat{\mathbf{I}} = \mathbf{xx} + \mathbf{yy} + \mathbf{zz}$ is the unit dyadic. Using the identity

$$\nabla\times\nabla\times = \nabla\nabla - \hat{\mathbf{I}}\Delta,$$

the Gauss's law

$$\nabla\mathbf{E}(\mathbf{r},\omega) = 4\pi\rho(\mathbf{r},\omega),$$

the equation of continuity

$$\nabla\mathbf{j}(\mathbf{r},\omega) = i\omega\rho(\mathbf{r},\omega), \tag{B5}$$

and Eq. (B2), Eq. (B4) becomes

$$\{\Delta + K_0^2\}\mathbf{E}(\mathbf{r},\mathbf{r}',\omega) = -4\pi\{\nabla\nabla + K_0^2\hat{\mathbf{I}}\}\delta(\mathbf{r}-\mathbf{r}')\mathbf{P}_0, \quad \text{(B6)}$$

where $K_0^2 = \frac{\omega^2}{c^2}$. After three-dimensional Fourier transformation Eq. (B6) becomes

$$E_\mu(\mathbf{r},\mathbf{r}',\omega) = 4\pi\int \frac{d^3\mathbf{k}}{(2\pi)^3}\frac{-k_\mu k_\nu + K_0^2\delta_{\mu\nu}}{k^2 - K_0^2}P_0^\nu e^{i\mathbf{k}(\mathbf{r}-\mathbf{r}')}, \quad \text{(B7)}$$

which can also be written as

$$\mathbf{E}(\mathbf{r},\mathbf{r}',\omega) = 4\pi\{\nabla\nabla + K_0^2\hat{\mathbf{I}}\}\int \frac{d^3\mathbf{k}}{(2\pi)^3}\frac{e^{i\mathbf{k}(\mathbf{r}-\mathbf{r}')}}{k^2 - K_0^2}\mathbf{P}_0. \quad \text{(B8)}$$

After integrating over k_z and calculating the gradients, we see that the Fourier component of $\mathbf{E}(\mathbf{r},\mathbf{r}',\omega)$ can be written as

$$\mathbf{E}(Q,\omega,z,z') = \left[-4\pi\delta(z-z')\mathbf{zz} + \frac{2\pi i K_0^2}{k_\perp}\{\mathbf{e}_s\mathbf{e}_s + \mathbf{e}_p\mathbf{e}_p\}e^{ik_\perp|z-z'|}\right]\mathbf{P}_0. \quad \text{(B9)}$$

Finally, comparing Eqs. (B3) and (B9) we get the explicit expression for the free-space electromagnetic-field propagator

$$\hat{\mathbf{D}}^0(Q,\omega,z,z') = -\frac{4\pi c}{\omega^2}\delta(z-z')\mathbf{zz} + \frac{2\pi i}{ck_\perp}\{\mathbf{e}_s\mathbf{e}_s + \mathbf{e}_p\mathbf{e}_p\}e^{ik_\perp|z-z'|}. \quad \text{(B10)}$$

Here unit vectors $\mathbf{e}_s = \mathbf{Q}_0 \times \mathbf{z}$ and $\mathbf{e}_p = \frac{1}{K_0}[-k_\perp\, sgn(z-z')\mathbf{Q}_0 + Q\mathbf{z}]$, with $\mathbf{Q}_0$ being the unit vector in $\mathbf{Q}$ direction and $k_\perp = \sqrt{K_0^2 - Q^2}$, give directions of $\mathbf{s}$(TE) and $\mathbf{p}$(TM)-polarized field components, respectively. If we choose the coordinate system so that $\mathbf{Q}_0 = \mathbf{y}$ (unit vector in y direction), we get the tensor $\hat{\mathbf{D}}^0$ in the explicit form presented in Eqs. (21)–(25).

*vito@phy.hr
†msunjic@phy.hr
‡lmarusic@unizd.hr

[1] R. H. Ritchie, Phys. Rev. **106**, 874 (1957).
[2] R. A. Ferrell, Phys. Rev. **111**, 1214 (1958).
[3] E. N. Economou, Phys. Rev. **182**, 539 (1969).
[4] P. J. Feibelman, Phys. Rev. B **12**, 1319 (1975).
[5] N. D. Lang and W. Kohn, Phys. Rev. B **1**, 4555 (1970).
[6] P. J. Feibelman, Phys. Rev. B **14**, 762 (1976).
[7] O. Keller, Phys. Rev. B **34**, 3883 (1986).
[8] O. Keller and A. Liu, Phys. Rev. B **49**, 2072 (1994).
[9] O. Keller and A. Liu, Phys. Scr. **51**, 531 (1995).
[10] F. A. Pudonin, R. Villagomez, and O. Keller, Opt. Commun. **170**, 181 (1999).
[11] O. Keller, Phys. Rev. B **48**, 4786 (1993); X. Chen and O. Keller, *ibid.* **55**, 15706 (1997).
[12] J. S. Nkoma, J. Phys.: Condens. Matter **1** 9623 (1989); F. J. Garcia-Vidal and J. B. Pendry, Phys. Rev. Lett. **77**, 1163 (1996).
[13] A. T. Georges, Phys. Rev. B **51**, 13735 (1995); V. M. Shalaev, C. Douketis, T. Haslett, T. Stuckless, and M. Moskovits, *ibid.* **53**, 11193 (1996).
[14] T. Andersen and O. Keller, Phys. Rev. B **57**, 14793 (1998); Phys. Scr. **58**, 132 (1998); Opt. Commun. **155**, 317 (1998) Phys. Rev. B **60**, 17046 (1999).
[15] I. Gontijo, M. Boroditsky, E. Yablonovitch, S. Keller, U. K. Mishra, and S. P. DenBaars, Phys. Rev. B **60**, 11564 (1999).
[16] A. Neogi, C.-W. Lee, H. O. Everitt, T. Kuroda, A. Tackeuchi, and E. Yablonovitch, Phys. Rev. B **66**, 153305 (2002).
[17] K. Okamoto, I. Niki, A. Scherer, Y. Narukawa, T. Mukai, and Y. Kawakami, Appl. Phys. Lett. **87**, 071102 (2005).
[18] P. T. Worthing, R. M. Amos, and W. L. Barnes, Phys. Rev. A **59**, 865 (1999).
[19] K. Vasilev, W. Knoll, and M. Kreiter, J. Chem. Phys. **120**, 3439 (2004).
[20] Y. Y. Zhai, H. Song, Z.-H. Zhou, M. Li, and Z.-H. Hao, Eur. Phys. J.: Appl. Phys. **42**, 109 (2008).
[21] S. Kuhn, U. Hakanson, L. Rogobete, and V. Sandoghdar, Phys. Rev. Lett. **97**, 017402 (2006).
[22] Yi. Fu and Joseph R. Lakowicz, Plasmonic Short. Comm. **2**, 1 (2007).
[23] Y. Zhang, K. Aslan, M. J. R. Previte, and C. D. Geddes, Appl. Phys. Lett. **90**, 053107 (2007).
[24] E. Dulkeith, A. C. Morteani, T. Niedereichholz, T. A. Klar, J. Feldmann, S. A. Levi, F. C. J. M. van Veggel, D. N. Reinhoudt, M. Moller, and D. I. Gittins, Phys. Rev. Lett. **89**, 203002 (2002).
[25] Z. Gueroui and Albert Libchaber, Phys. Rev. Lett. **93**, 166108 (2004).
[26] P. Anger, P. Bharadwaj, and L. Novotny, Phys. Rev. Lett. **96**, 113002 (2006).
[27] P. T. Leung, Y. S. Kim, and T. F. George, Phys. Rev. B **39**, 9888 (1989).
[28] D. E. Chang, A. S. Sorensen, P. R. Hemmer, and M. D. Lukin, Phys. Rev. B **76**, 035420 (2007).
[29] I. A. Larkin, M. I. Stockman, M. Achermann, V. I. Klimov, Phys. Rev. B **69**, 121403(R) (2004).
[30] H. Morawitz and M. R. Philpott, Phys. Rev. B **10**, 4863 (1974).
[31] G. W. Ford and H. Weber, Phys. Rep. **113**, 195 (1984).
[32] V. M. Silkin, E. V. Chulkov, and P. M. Echenique, Phys. Rev. Lett. **93**, 176801 (2004).
[33] V. M. Silkin, E. V. Chulkov, and P. M. Echenique, Radiat. Eff. Defects Solids **162**, 483 (2007).
[34] V. M. Silkin, J. M. Pitarke, E. V. Chulkov, and P. M. Echenique, Phys. Rev. B **72**, 115435 (2005).
[35] B. Diaconescu, K. Pohl, L. Vattuone, L. Savio, P. Hofmann, V. M. Silkin, J. M. Pitarke, E. V. Chulkov, P. M. Echenique, D. FarÃas, and M. Rocca, Nature (London) **448**, 57 (2007).
[36] A. Bergara, V. M. Silkin, E. V. Chulkov, and P. M. Echenique, Phys. Rev. B **67**, 245402 (2003).
[37] L. Marušić and M. Šunjić, Phys. Scr. **63**, 336 (2001).

[38] L. Marušić, V. Despoja, and M. Šunjić, J. Phys.: Condens. Matter **18**, 4253 (2006).
[39] M. S. Tomaš, Phys. Rev. A **51**, 2545 (1995).
[40] F. K. Schulte, Surf. Sci. **55**, 427 (1976).
[41] I. Kupčić and S. Barišić, Fiz. A **14**, 47 (2005).
[42] A. A. Abrikosov, L. P. Gorkov, and I. E. Dzyaloshinski, *Methods of Quantum Field Theory in Statistical Physics* (Prentice-Hall, Englewood Cliffs, NJ, 1963), Chap. 6.
[43] V. Despoja, L. Marušić, and M. Šunjić, Solid State Commun. **140**, 270 (2006).
[44] V. M. Silkin, A. Balassis, P. M. Echenique, and E. V. Chulkov, arXiv:0805.1558 (unpublished).
[45] E. V. Chulkov, V. M. Silkin, and P. M. Echenique, Surf. Sci. **437**, 330 (1999).
[46] A. G. Eguiluz, Phys. Rev. Lett. **51**, 1907 (1983).
[47] Z. Penzar and M. Šunjić, Phys. Scr. **30**, 431 (1984).